Loss of Flower/FLWR-1 induces an increase in neuronal excitability and causes defective recycling of synaptic vesicles

Marius Seidenthal[1,2], Jasmina Redzovic[1,2,3,4], Jana F. Liewald[1,2,4], Dennis Rentsch[1,2], Stepan Shapiguzov[1,2], Noah Schuh[1,2], Stefan Eimer[3], Alexander Gottschalk[*,1,2]

[1] Buchmann Institute for Molecular Life Sciences, Goethe-University, Max-von-Laue-Strasse 15, 60438 Frankfurt am Main, Germany

[2] Institute for Biophysical Chemistry, Department of Biochemistry, Chemistry, and Pharmacy, Goethe-University, Max-von-Laue-Strasse 9, 60438 Frankfurt am Main, Germany

3 Institute of Cell Biology and Neuroscience, Goethe-University, Max-von-Laue-Strasse 13, 60438 Frankfurt am Main, Germany

4 Contributed equally

*** to whom correspondence should be addressed:** a.gottschalk@em.uni-frankfurt.de

Keywords: neurotransmission, synaptic vesicles, exo-endocytosis, *Caenorhabditis elegans*, synaptic plasticity, excitation-inhibition imbalance

Abstract

The Flower protein is proposed to couple synaptic vesicle fusion to recycling in different model organisms. It is supposed to trigger activity-dependent bulk endocytosis by conducting Ca^{2+} at endocytic sites. However, this mode of action is debated. Here, we investigate the role of the nematode homolog (FLWR-1) in neurotransmission in *Caenorhabditis elegans*. Our results confirm that FLWR-1 facilitates the recycling of synaptic vesicles at the neuromuscular junction. Ultrastructural analysis of synaptic boutons after hyperstimulation surprisingly reveals an accumulation of endosomal structures in *flwr-1* mutants. These findings do not support a role of FLWR-1 in the formation of bulk endosomes but rather a function in their breakdown following cleavage from the plasma membrane. Unexpectedly, loss of FLWR-1 conveys increased neuronal excitability which causes an excitation-inhibition imbalance. Finally, we obtained evidence that this increased transmission at the neuromuscular junction might be caused by deregulation of MCA-3, the nematode homolog of the plasma membrane Ca^{2+} ATPase (PMCA).

Introduction

Chemical synaptic transmission involves a cycle of biogenesis of synaptic vesicles (SVs), their fusion with the plasma membrane (PM), as well as their recycling by endocytosis and de novo formation in the endosome. Coupling of SV exocytosis and endocytosis must be tightly controlled to avoid depletion of the reserve pool of SVs and to enable sustained neurotransmission (Haucke et al., 2011; Lou, 2018). Different hypotheses have been formulated as to how this is achieved within neurons. One hypothesis suggests that an SV-integral transmembrane protein called Flower could form ion channels and gets inserted into the PM during SV fusion (Yao et al., 2009). Subsequently, it may facilitate endocytosis by conducting Ca^{2+} into the cytoplasm, thus contributing to defining endocytic sites (Yao et al., 2017). In *Drosophila melanogaster*, Flower was proposed to increase phosphatidylinositol-4,5-bisphosphate ($PI(4,5)P_2$) levels through Ca^{2+} microdomains, which was suggested to drive activity-dependent bulk endocytosis (ADBE) and formation of new SVs after prolonged, intense neurotransmission (Li et al., 2020). The hypothesis that Flower may have Ca^{2+} channel activity was further proposed based on sequence similarities between Flower and the Ca^{2+} selectivity filter of voltage-gated Ca^{2+} channels (VGCCs; Yao et al. (2009)). Additional evidence from *Drosophila* suggests that Flower may regulate clathrin-mediated endocytosis (CME) in a Ca^{2+} independent fashion (Yao et al., 2017). However, while a facilitatory role of Flower in endocytosis appears to be evolutionarily conserved, and was observed in different organisms and tissues, including non-neuronal cells (Yao et al., 2017; Chang et al., 2018; Rudd et al., 2023), its Ca^{2+} channel activity and its influence on SV recycling is debated (Lou,

2018; Coelho and Moreno, 2020). The kinetics of Ca^{2+} influx mediated by Flower appear to be too slow and the amount conducted too low to have a major impact (Xue et al., 2012). The function of Flower and its dependence on Ca^{2+} moreover seem to be highly dependent on the cell type and the extent of synaptic activity (Yao et al., 2017; Chang et al., 2018). Apart from its role in endocytosis, Flower is involved in cell survival mechanisms during development (Coelho and Moreno, 2020; Costa-Rodrigues et al., 2021). Intriguingly, loss of the mammalian homolog of Flower can reduce tumor growth, suggesting an important function in tumor cell survival and introducing possible options for cancer treatment (Petrova et al., 2012; Madan et al., 2019). However, sufficient research of the exact signaling pathways by means of which Flower mediates cell survival is lacking (Costa-Rodrigues et al., 2021).

Studies which address this mechanism usually propose a two- or three-transmembrane domain organization of the Flower protein structure in which the C-terminus is exposed to the extracellular space and can thus be used for intercellular communication (Rhiner et al., 2010; Costa-Rodrigues et al., 2021). However, more recent research has shown that both N- and C-terminal tails of Flower are likely cytosolic and the longest mammalian isoforms consists of four transmembrane helices which are connected by short loops (Chang et al., 2018; Rudd et al., 2023). The genome of nematodes is predicted to contain only a single isoform of Flower (FLWR-1; *wormbase.org*). They therefore serve as excellent model organisms to further investigate the evolutionarily conserved role of Flower in neurotransmission and endocytosis. Here, we studied the function of FLWR-1 in the nematode *Caenorhabditis elegans*. We find that FLWR-1 localizes to SVs and to the PM and is involved in neurotransmission. We further show that FLWR-1 has a facilitatory but not essential role in endocytosis, confirming previous research in *Drosophila* and mammalian cells. Loss of FLWR-1 surprisingly conveys increased excitability of motor neurons and neurotransmitter release suggesting a deregulation of Ca^{2+} signaling in the presynapse. This is associated with defective SV recycling at the level of the endosome and thus reduced SV numbers upon sustained stimulation. This excitability change is more pronounced in γ-aminobutyric acid (GABA)ergic neurons and leads to an excitation-inhibition (E/I) imbalance at the neuromuscular junction (NMJ) through increased release of the neurotransmitter GABA. A function of FLWR-1 in endocytosis appears to affect also the plasma membrane Ca^{2+}-ATPase MCA-3, required for extrusion of Ca^{2+} from the cytosol, and may thus explain the increased excitability observed in *flwr-1* mutant neurons.

Materials and methods

Molecular biology

An overview of plasmids used in this paper and how they were generated can be found in **Supplementary Table 1**. **pZIM902** [punc-17b::GCaMP6fOpt] was a gift from Manuel Zimmer. **p1676** [punc-17(short)::TagRFP::ELKS-1] was kindly provided by the lab of Zhao-Wen Wang. **pJH2523** [punc-25::GCaMP3::UrSL2::wCherry] was a gift from Mei Zhen (Addgene plasmid # 191358 ; http://n2t.net/addgene:191358 ; RRID:Addgene_191358) (Lu et al., 2022).

Cultivation of *C. elegans*

Animals were kept at 20 °C on nematode growth medium (NGM) plates seeded with OP50-1 bacteria (Brenner, 1974). For optogenetic experiments, OP50-1 was supplemented with 200 µM ATR prior to seeding and animals were kept in darkness. Transgenic animals carrying extrachromosomal arrays were generated by microinjection into the gonads (Fire, 1986). L4 staged larvae were picked ~18 h before experiments and tested on at least three separate days with animals picked from different populations. Transgenic animals were selected by fluorescent markers using a Leica MZ16F dissection stereo microscope. Integration of the *sybIs8965* transgenic array (PHX8965 strain) was performed by SunyBiotech. The RB2305 strain containing the *flwr-1(ok3128)* allele was outcrossed three times with N2 wild type animals. An overview of strains with their respective genotypes and transgenes can be found in **Supplementary Table 2**.

Counting live progeny

To count living progeny per animal, five L4 larvae were singled onto NGM plates seeded with 50 µl OP50-1. Animals were then picked onto fresh plates after two days and on each of the following two days and removed on day five. Living progeny per animal was counted after reaching adulthood and summed up over the three plates each animal laid eggs on, respectively. Experiments were performed blinded to the genotype.

88 **Pharmacological assays**

89 1.5 mM aldicarb and 0.25 levamisole plates were prepared by adding the compounds to liquid NGM prior to plate pouring (Mahoney et al.,
90 2006). Aldicarb (Sigma Aldrich, USA) was kept as a 100 mM stock solution in 70 % ethanol. Levamisole (Sigma Aldrich, USA) was stored
91 as a 200 mM solution dissolved in ddH_2O. 15 - 20 young adult animals were transferred to each plate and tested every 15 (levamisole) or
92 30 (aldicarb) minutes. Assays were performed blinded to the genotype and control groups (wild type and *flwr-1* mutants) were measured
93 in parallel on the same day. Animals that did not respond after being prodded three times with a hair pick were counted as paralyzed. Worms
94 that crawled of the plate were disregarded from analysis.

95 **Measurement of swimming speed using the multi-worm-tracker (MWT)**

96 Swimming speed was measured as described previously (Vettkotter et al., 2022). In short, worms were washed three times with M9 buffer
97 to remove OP50 and transferred onto 3.5 cm NGM plates with 800 µl M9. Animals were visualized using the multiworm tracker (MWT)
98 platform (Swierczek et al., 2011) equipped with a Falcon 4M30 camera (DALSA). Channelrhodopsin-2 (ChR2) was stimulated with 470
99 nm light at 1 mW/mm^2 intensity for 90 s. 30 s videos were captured and thrashing was analyzed using the "wrmTrck" plugin for ImageJ
100 (Nussbaum-Krammer et al., 2015). The automatically generated tracks were validated using a custom written Python script
101 (https://github.com/dvettkoe/SwimmingTracksProcessing).

102 **Measurement of body length**

103 Body length was measured as described previously (Liewald et al., 2008; Seidenthal et al., 2022). In short, single animals were transferred
104 onto unseeded NGM plates and illuminated with light from a 50 W HBO lamp which was filtered with a 450 - 490 nm bandpass excitation
105 filter. ChR2 was stimulated with 100 $\mu W/mm^2$ light intensity. A 665 - 715 nm filter was used to avoid unwanted activation by brightfield
106 light. Body length was analyzed using the "WormRuler" software (version 1.3.0) and normalized for the average skeleton length before
107 stimulation (Seidenthal et al., 2022). Values which are more than 20 % higher or lower than the initial body length were discarded as they
108 result from artifacts in the background correction and are biomechanically unlikely. Basal body length was calculated from the skeleton
109 length in pixels which is generated by the WormRuler software. This was converted to mm and averaged for each animal over a duration
110 of five seconds.

111 **Light microscopy and quantification of fluorescence**

112 Animals were placed upon 7 % agarose pads in M9 buffer. Worms were immobilized by either using 20 mM levamisole in M9 or Polybead
113 polystyrene microspheres (Polysciences) for experiments involving GABAergic stimulation. For optogenetic experiments, single animals
114 were placed upon pads to avoid unwanted pre-activation of channelrhodopsins. Imaging was performed using a Axio Observer Z1
115 microscope (Zeiss, Germany). Proteins were excited using 460 nm and 590 nm LEDs (Lumen 100, Prior Scientific, UK) coupled via a
116 beamsplitter. Background correction was conducted by placing a region of interest (ROI) within the animal yet avoiding autofluorescence.

117 GCaMP and pHluorin imaging and ChrimsonSA stimulation was performed using a 605 nm beamsplitter (AHF Analysentechnik, Germany)
118 which was combined with a double band pass filter (460 - 500 and 570 - 600 nm). A single bandpass emission filter was used (502.5 - 537.5
119 nm). pOpsicle assays were performed as described previously using a 100-x objective (Seidenthal et al., 2023). We extended the
120 ChrimsonSA stimulation light pulse to 30 s to be consistent with the stimulus length of electron microscopy (EM) and electrophysiology
121 experiments. Moreover, 2 x 2 binning was applied. Image sequences with 200 ms light exposure (5 frames per second) were acquired with
122 an sCMOS camera (Kinetix 22, Teledyne Photometrics, USA). Video acquisition was controlled using the µManager v.1.4.22 software
123 (Edelstein et al., 2014). The timing of LED activation was managed using a *Autohotkey* script. GCaMP imaging was conducted similarly
124 with the same setup and light intensity for ChrimsonSA stimulation (40 $\mu W/mm^2$) yet without binning. Dorsal nerve cord (DNC)
125 fluorescence was quantified with ImageJ by placing a region of interest ROI with the *Segmented Line* tool. XY-drift was corrected using
126 the *Template Matching* plugin if necessary. Animals showing excessive z-drift were discarded. A custom written python script was used to
127 summarize background subtraction and normalization to the average fluorescence before pulse start
128 (https://github.com/MariusSeidenthal/pHluorin_Imaging_Analysis). For GCaMP imaging, the bleach correction function of this python
129 script was used which corrects fluorescence traces with strong bleaching. Strong bleaching is defined as the fluorescence intensity of the
130 mean of the last second of measurement being less than 85% of the first second. The script performs linear regression analysis for DNC
131 fluorescent traces and background ROI and corrects values prior to background correction. The increase in GCaMP fluorescence during
132 stimulation was highly dependent on basal fluorescence values before stimulation and transient Ca^{2+} signals. This caused some
133 measurements to show very strong increases in fluorescence. To avoid distortion of statistical analyses, we performed outlier detection for
134 the increase during stimulation on all datasets with the Graphpad Prism 9.4.1 Iterative Grubb's method. The alpha value (false discovery
135 rate) was set to 0.01. For pOpsicle assays, animals were screened for whether they show a significant increase in fluorescence during
136 stimulation, which is necessary for analysis of fluorescence decay after stimulation. A strong signal was determined as the maximum
137 background corrected fluorescence during the light pulse (moving average of 5 frames) being larger than the average before stimulation +
138 3 times the standard deviation of the background corrected fluorescence before stimulation. Regression analysis of pHluorin fluorescence

decay was performed as described previously by using Graphpad Prism 9.4.1 and fitting a "Plateau followed one-phase exponential decay" fit beginning with the first time point after stimulation to single measurements (Seidenthal et al., 2023). Animals that displayed no increase during stimulation as well as animals showing no decay or spontaneous signals after stimulation were discarded from analysis.

Comparison of dorsal and ventral (VNC) nerve cord fluorescence of GFP::FLWR-1 and mCherry::SNB-1 was conducted by imaging the posterior part of the animal where an abundance of synapses can be found. Images were acquired using the same beamsplitter and excitation filter as used for pOpsicle experiments but equipped with a 500 – 540 nm/600 – 665 nm double bandpass emission filter (AHF Analysentechnik, Germany) and 2 x 2 binning. The Arduino script "AOTFcontroller" was used to control synchronized 2-color illumination (Aoki et al., 2023). VNC and DNC fluorescence were analyzed by choosing single frames from acquired z-stacks in which nerve cords were well focused. Fluorescence intensities were quantified by placing a *Segmented Line* ROI. Kymographs were generated with the ImageJ *Multi Kymograph* function.

Confocal laser scanning microscopy was performed on a LSM 780 microscope (Zeiss, Germany) equipped with a Plan-Apochromat 63-x oil objective. The Zeiss Zen (blue edition) *Tile Scan* and *Z-Stack* functions were used to generate overview images of animals expressing GFP::FLWR-1. Images were processed and maximum z-projection performed using ImageJ. Colocalization analysis was performed by placing a *Segmented Line* ROI onto the DNC and plotting the fluorescence profile along the selected ROI for both color channels. Correlation of fluorescence intensities was then conducted using the GraphPad Prism 9.4.1 Pearson correlation function.

Fluorescence of GFP taken up by coelomocytes was visualized with a 40-x objective. An eGFP filter cube (AHF Analysentechnik, Germany) was used and fluorescence was excited with the 460 nm LED. Images were acquired using 50 ms exposure and 2 x 2 binning. Fluorescence was quantified by drawing a ROI around all coelomocytes found within any worm imaged using the *Freehand selections* tool and performing background correction. Coelomocyte fluorescence was then averaged for each animal.

Electrophysiology

Electrophysiological recordings of body wall muscle cells (BWMs) were done in dissected adult worms as previously described (Liewald et al., 2008). Animals were immobilized with Histoacryl L glue (B. Braun Surgical, Spain) and a lateral incision was made to access NMJs along the anterior VNC. The basement membrane overlying BWMs was enzymatically removed by 0.5 mg/ml collagenase for 10 s (C5138, Sigma-Aldrich, Germany). Integrity of BWMs and nerve cord was visually examined via DIC microscopy.

Recordings from BWMs were acquired in whole-cell patch-clamp mode at 20-22 °C using an EPC-10 amplifier equipped with Patchmaster software (HEKA, Germany). The head stage was connected to a standard HEKA pipette holder for fire-polished borosilicate pipettes (1B100F-4, Worcester Polytechnic Institute, USA) of 4–10 MΩ resistance. The extracellular bath solution consisted of 150 mM NaCl, 5 mM KCl, 5 mM $CaCl_2$,1 mM $MgCl_2$,10 mM glucose, 5 mM sucrose, and 15 mM HEPES, pH 7.3, with NaOH, ~330 mOsm. The internal/patch pipette solution consisted of K-gluconate 115 mM, KCl 25 mM, $CaCl_2$ 0.1 mM, $MgCl_2$ 5 mM, BAPTA 1 mM, HEPES 10 mM, Na_2ATP 5 mM, Na_2GTP 0.5 mM, cAMP 0.5 mM, and cGMP 0.5 mM, pH 7.2, with KOH, ~320 mOsm.

Voltage clamp experiments were conducted at a holding potential of −60 mV. Light activation was performed using an LED lamp (KSL-70, Rapp OptoElectronic, Hamburg, Germany; 470 nm, 8 mW/mm²) and controlled by the Patchmaster software. Subsequent analysis was performed using Patchmaster and Origin (Originlabs). Analysis of mPSCs was conducted with MiniAnalysis (Synaptosoft, Decatur, GA, USA, version 6.0.7) and rate and amplitude of mPSCs was analyzed in 1 s bins. Exponential decay of mPSCs during stimulation was calculated with Graphpad Prism 9.4.1 by fitting a one-phase exponential decay beginning with the first time point during stimulation.

Transmission electron microscopy

Prior to high-pressure freezing (HPF), L4 animals were transferred to freshly seeded *E. coli* OP50-1 dishes supplemented with or without 0.1 mM ATR. HPF fixation was performed on young adult animals as described previously (Weimer, 2006; Kittelmann et al., 2013b). Briefly, 20 - 40 animals were transferred into a 100 µm deep aluminum planchette (Microscopy Services) filled with *E. coli* (supplemented with or without ATR, respectively), covered with a sapphire disk (0.16 mm) and a spacer ring (0.4 mm; engineering office M. Wohlwend) for photostimulation. To prevent pre-activation of ChR2, all preparations were carried out under red light. Animals were continuously illuminated for 30 s with a laser (470 nm, ~20 mW/mm²) followed by HPF at -180 °C under 2100 bar pressure in an HPM100 (Leica Microsystems). Frozen specimens were transferred under liquid nitrogen into a Reichert AFS machine (Leica Microsystems) for freeze substitution. Samples were incubated with tannic acid (0.1% in dry acetone) fixative at -90 °C for 100 h. Afterward, a process of washing was performed for substitution with acetone, followed by incubation of the samples in 2% OsO_4 (in dry acetone) for 39.5 h while the temperature was slowly increased up to room temperature. Subsequently, samples were embedded in epoxy resin (Agar Scientific, AGAR 100 Premix kit – hard) by increasing epoxy resin concentrations from 50% to 90% at room temperature and 100% at 60 °C for 48 h. Electron micrographs of 2 - 5individual animals, and from 12 – 22 synapses per treatment, were acquired by cutting cross sections at a thickness of 40 nm, transferring cross sections to formvar- or pioloform covered copper slot grids. Specimens were counterstained in 2.5% aqueous uranyl acetate for 4 min, followed by washing with distilled water, and incubation in Reynolds lead citrate solution for 2 min in a CO_2-free chamber with subsequent washing steps in distilled water. VNC regions were then imaged with a Zeiss 900 TEM, operated at 80 kV, with

a Troendle 2K camera. Images were scored and tagged blind in ImageJ (version 1.53c, National Institute of Health) as described previously, and analyzed using SynapsEM (Watanabe et al., 2020; Vettkotter et al., 2022). Since the number of synaptic organelles varied between synapses of different sizes, their counts were normalized to the average synaptic profile area of 145,253 nm^2. Endosomes are defined as structures larger than 100 nm and located more than 50 nm away from the dense projection, as described by (Watanabe et al., 2014). Irregular vesicular structures exceeding 100 nm in either height or width were also included.

Protein alignment and structure prediction

Protein alignment was performed with ClustalX (Larkin et al., 2007) and shading of conserved residues created with Boxshade (*https://junli.netlify.app/apps/boxshade/*). Transmembrane domains as well as membrane orientation were predicted by entering the predicted amino acid sequence to DeepTMHMM (Hallgren et al., 2022). FLWR-1 structure was modeled and visualized with Alphafold3 (AF3) (Abramson et al., 2024). FLWR-1 tetramers have been modeled using AlphafoldMultimer or AF3 (Evans et al., 2022). Protein structures were analyzed and edited using PyMol v2.5.2. Docking of $PI(4,5)P_2$ to the FLWR-1 AF3 model was conducted in PyMol using the DockingPie plugin running the Autodock/Vina analysis (Eberhardt et al., 2021; Rosignoli and Paiardini, 2022).

Statistical Analysis and generation of graphs

Graphs were created and statistical analyses were performed using GraphPad Prism 9.4.1. Data was displayed as mean ± standard error of the mean (SEM) unless noted otherwise. Unpaired t-tests were used to compare two datasets and one-way ANOVAs or two-way ANOVAs if three or more datasets were assessed, according to the number of tested conditions. Fitting of a mixed-effects model was used instead of two-way ANOVA if the number of data points was not constant between different datasets for example if the number of animals differed between time points. Mann-Whitney tests were performed if two datasets were compared that were not normally distributed and datasets were depicted as median with interquartile range (IQR) in statistical analyses. Kruskal-Wallis tests were conducted if not normally distributed datasets were assessed. Iterative Grubb's outlier detection was used when required and as indicated. The alpha value (false discovery rate) was set to 0.01. Representations of the exon-intron structures of genes were created using the "Exon-Intron Graphic Maker" (Bhatla, 2012).

Results

FLWR-1 is involved in neurotransmission.

The amino acid sequence of *C. elegans* FLWR-1 is conserved to its *D. melanogaster* (Fwe-Ubi) and *Homo sapiens* (hFwe4) homologues (**Fig. 1A**). Fwe-Ubi has been shown to facilitate recovery of neurons following intense synaptic activity (Yao et al., 2009; Yao et al., 2017). To investigate whether this involvement of Flower in neurotransmission is evolutionarily conserved, we studied a mutant lacking most of the *flwr-1* coding region (*ok3128*, **Fig. 1B**) (Consortium, 2012). Animals lacking FLWR-1 did not display severe phenotypic differences to wild type animals. Basal locomotion in liquid (**Fig. 1C, D** seconds 0 – 30) and body length of young adults (**Fig. S1A**) were not significantly different from the respective values of wild type animals. However, fertility appeared slightly reduced (**Fig. S1B**). Thus, it is likely that FLWR-1 does not have an essential function in neurotransmission but rather a regulatory or facilitatory role. Previous studies have shown that mutations which only weakly affect basal locomotion, can display severely reduced recovery of swimming speed after strong optogenetic stimulation of cholinergic neurons (Yu et al., 2018). We therefore subjected *flwr-1(ok3128)* mutants expressing channelrhodopsin-2(H134R), which were treated with the chromophore all-*trans* retinal (ATR), to blue light during swimming (Nagel et al., 2005; Liewald et al., 2008). Photostimulation resulted in a stop of all swimming during the light pulse, followed by a slow recovery in the dark. Indeed, loss of FLWR-1 led to a significantly slowed recovery of swimming locomotion (**Fig. 1C, D**). This could be fully rescued by transgenic expression of genomic FLWR-1 including a two kilobase sequence upstream of the putative start codon, hereafter called *pflwr-1* (as the promoter of *flwr-1*). To further evaluate the involvement of FLWR-1 in neurotransmission, we exposed *flwr-1* mutants to aldicarb. This acetylcholine esterase inhibitor induces paralysis due to accumulation of acetylcholine in the synaptic cleft (Mahoney et al., 2006; Blazie and Jin, 2018). Resistance to aldicarb indicates either reduced release or reception of acetylcholine or increased inhibitory signaling (Vashlishan et al., 2008; Janosi et al., 2024). Loss of FLWR-1 led to a significant delay in paralysis indicating involvement in transmission at the NMJ (**Fig. 1E**). Full rescue of the *flwr-*

1 mutant phenotypes suggests that expression from the 2 kB fragment of the endogenous promoter fully recapitulates the native expression in the context of NMJ function.

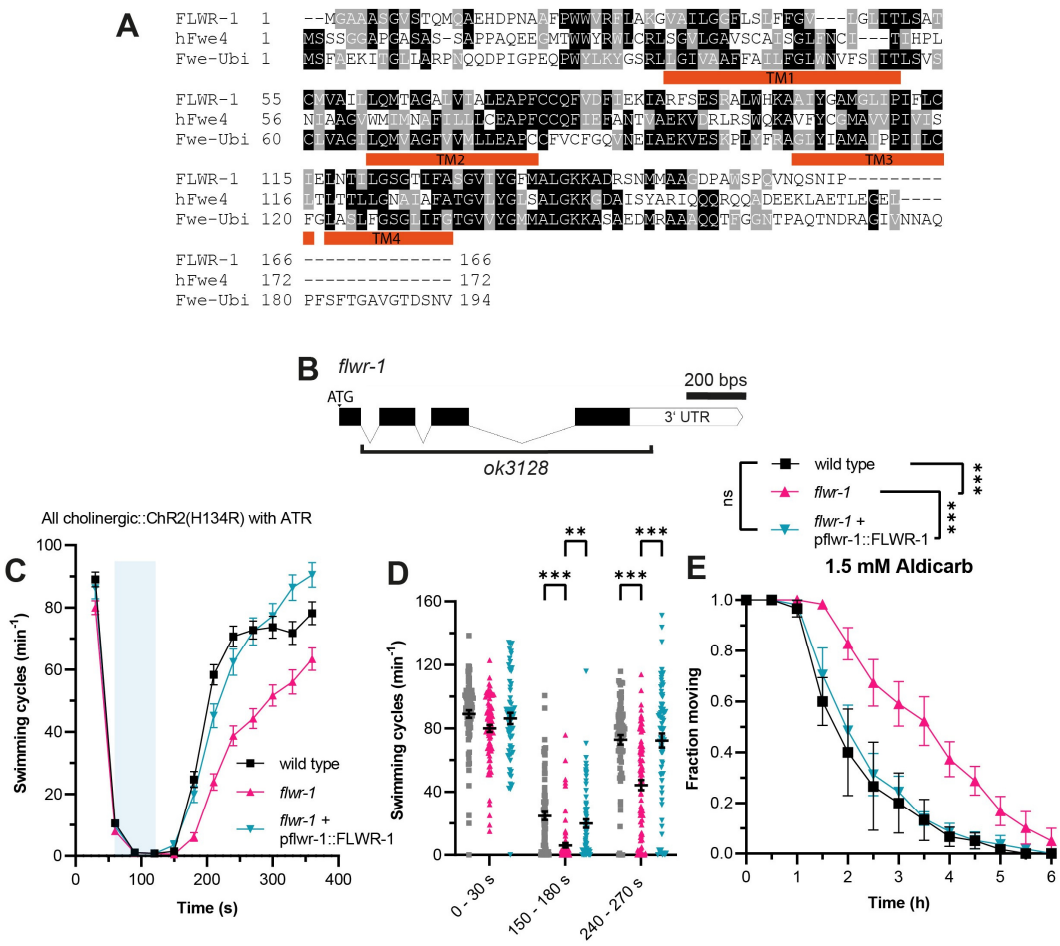

Fig. 1. Loss of FLWR-1 induces defects in neuro-transmission fol-lowing intense stimulation.

(A) Alignment of the amino acid sequences of FLWR-1 to hFwe4 (*Homo sapiens*) and Fwe-Ubi (*Drosophila melanogaster*). Shading depicts evolutionary conservation of amino acid residues (identity – black; homology – grey). **(B)** Schematic representation of the *flwr-1*/F20D1.1 gene locus and the size of the *ok3128* deletion. Bars represent exons and connecting lines introns. **(C)** Mean (± SEM) swimming cycles of animals expressing ChR2(H134R) in cholinergic motor neurons (*unc-17* promoter). All animals were treated with ATR. A 90 s light pulse (470 nm, 1 mW/mm^2) was applied after 30 s as indicated by the blue shade. Number of animals accumulated from N = 3 biological replicates: wild type = 80 – 88, *flwr-1* = 80 – 91, FLWR-1 rescue = 62 – 75. **(D)** Statistical analysis of swimming speed at different time points as depicted in (B). Mean (± SEM). Each dot represents a single animal. Mixed-effects model analysis with Tukey's correction. **(E)** Mean (± SEM) fraction of moving animals after exposure to 1.5 mM aldicarb. N = 4 biological replicates. Two-way ANOVA with Tukey's correction. ns not significant, *** $p < 0.001$.

FLWR-1 is expressed in excitable cells and localizes to synaptic vesicles.

Invertebrate and vertebrate homologues of FLWR-1 are predicted to be membrane proteins containing four transmembrane helices with both C- and N-termini located in the cytosol (Yao et al., 2009; Chang et al., 2018; Rudd et al., 2023). *In silico* predictions using the FLWR-1 sequence of 166 amino acids suggest evolutionary conservation of the tetraspan structure (**Fig. S2A**) (Hallgren et al., 2022). Accordingly, Alphafold3 prediction of FLWR-1 protein structure implies a four helical configuration, with helix lengths that could span biological membranes, and three additional, shorter α-helices (**Fig. S2B**) (Abramson et al., 2024). We sought to determine the cellular as well as subcellular localizations of FLWR-1 by tagging its C-terminus with GFP and expressing the construct using the endogenous promoter (**Fig. 2A – C**). Green fluorescence could be observed in developing embryos in the uterus, as well as in various tissues including neurons, body wall and pharyngeal muscles (**Fig. 2A**). FLWR-1 localized to neurites and cell bodies of nerve ring neurons, representing the central nervous system (brain) of the nematode (**Fig. 2B**) (Ward et al., 1975). These results are in accordance with single-cell RNA-sequencing data obtained from *C. elegans* which show near ubiquitous expression of *flwr-1/F20D1.1* (**Fig. S2C**, Supplementary Table 3; Taylor et al. (2021)). Within muscle cells, FLWR-1 was primarily targeted to the PM (**Fig. 2C**). As its *D. melanogaster* homolog was localized to synaptic vesicles (SVs) (Yao et al., 2009), we wondered whether FLWR-1 would colocalize with known SV markers such as synaptobrevin-1 (SNB-1) (Nonet, 1999; Calahorro and Izquierdo, 2018). Indeed, GFP::FLWR-1 fluorescence largely overlapped with co-expressed mCherry::SNB-1 in the dorsal nerve cord (DNC;

Fig. 2D, E). FLWR-1 further seemed to be enriched in fluorescent puncta in DNC and sublateral nerve cords indicating synaptic localization (**Fig. 2D - F**), however it was not restricted to synaptic regions only, meaning it is likely present also in the PM.

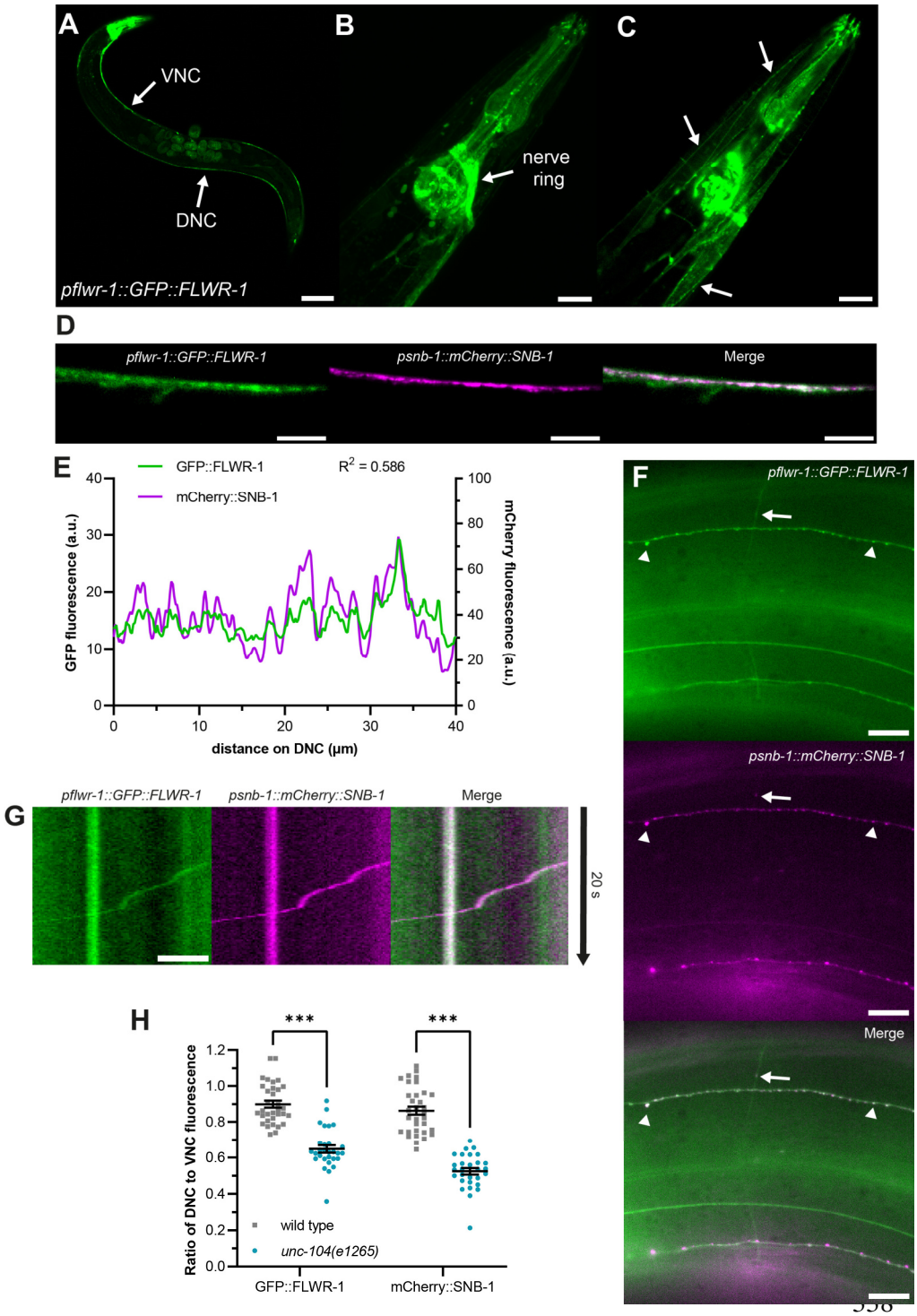

Fig. 2. FLWR-1 is expressed in neuronal cells and localizes to synaptic vesicles.

(A - D) Confocal micrographs (maximum projection of z-stacks or single plane) of animals co-expressing *pflwr-1::GFP::FLWR-1* and *psnb-1::mCherry::SNB-1*. **(A)** Overview of GFP::FLWR-1 expression. Arrows indicate dorsal (DNC) and ventral (VNC) nerve cords. Scale bar, 100 µm. **(B)** GFP::FLWR-1 in head neurons and pharynx. Scale bar, 20 µm. **(C)** Animal depicted in (B), single plane showing neck muscle cells. Arrows indicate GFP::FLWR-1 localization to the plasma membrane. Scale bar, 20 µm. **(D)** GFP and mCherry fluorescence in the DNC. Scale bar, 10 µm. **(E)** Line scan analysis of colocalization of GFP::FLWR-1 and mCherry::SNB-1 along the DNC as represented in (D). R^2 as determined by Pearson correlation. a.u. = arbitrary units of fluorescence intensity. **(F)** Micrograph depicting GFP::FLWR-1 and mCherry::SNB-1 fluorescence in sublateral nerve cords and commissures. Arrowheads indicate synaptic puncta. Arrow points towards SV precursor travelling along commissure as shown in Supplementary Movie 1. Scale bar, 10 µm. **(G)** Kymograph representing the SV precursor indicated in (F) travelling along commissures. Scale bar, 2 µm. **(H)** Comparison of the ratio of DNC to VNC fluorescence of GFP::FLWR-1 and mCherry::SNB-1 in wild type and *unc-104(e1265)* mutant background. Mean (± SEM). Each dot represents a single animal. Two-way ANOVA with Šídák's correction. *** $p < 0.001$. Number of animals imaged in N = 3 biological replicates: wild type = 33, *unc-104* = 29.

Furthermore, we observed moving particles, probably SV precursors, which contain SNB-1 and FLWR-1, travelling along commissures between ventral nerve cord (VNC) and DNC (**Fig. 2F, G** and Supplementary Movie 1). Anterograde transport of these precursors towards synapses has been shown to be dependent on kinesin-3/UNC-104

342 (Hall and Hedgecock, 1991; Klopfenstein and Vale, 2004). We used a strong reduction-of-function allele (*e1265*)
343 affecting interaction of UNC-104 with its cargo to investigate whether FLWR-1 is actively transported towards
344 synapses (Cong et al., 2021). Indeed, animals lacking functional UNC-104 showed a reduced amount of axonal GFP
345 fluorescence in the nerve ring and DNC while cell bodies were clearly visible (**Fig. S2D**). The ratio of DNC to VNC
346 fluorescence is significantly decreased in *unc-104* mutants suggesting defective anterograde transport (**Fig. 2H**).
347 Distribution of SNB-1 was similarly affected (Gally and Bessereau, 2003; Cuentas-Condori et al., 2023). Together,
348 these results argue that FLWR-1 is expressed in neurons (as well as in muscles and other cell types) and actively
349 transported towards synapses.

350 **GABAergic signaling is increased in *flwr-1* knockout mutants.**

351 Since FLWR-1 is also expressed in body wall muscles (BWMs), we wondered whether the observed aldicarb
352 resistance originates from reduced acetylcholine reception by acetylcholine receptors (AChR) (Mahoney et al.,
353 2006). To test this, we exposed animals lacking FLWR-1 to levamisole, an AChR agonist which induces paralysis
354 by hypercontraction, similar to aldicarb (Sattelle et al., 2002; Gottschalk et al., 2005). We found no significant
355 differences in the rate of paralysis between wild type and mutant animals (**Fig. S3A**). However, transgenic
356 expression of FLWR-1 in BWMs did rescue the aldicarb resistance partially (**Fig. S3B**). Therefore, loss of FLWR-
357 1 seems to decrease excitability of muscle cells in an aldicarb dependent context which may contribute to the aldicarb
358 resistance of *flwr-1* mutants.

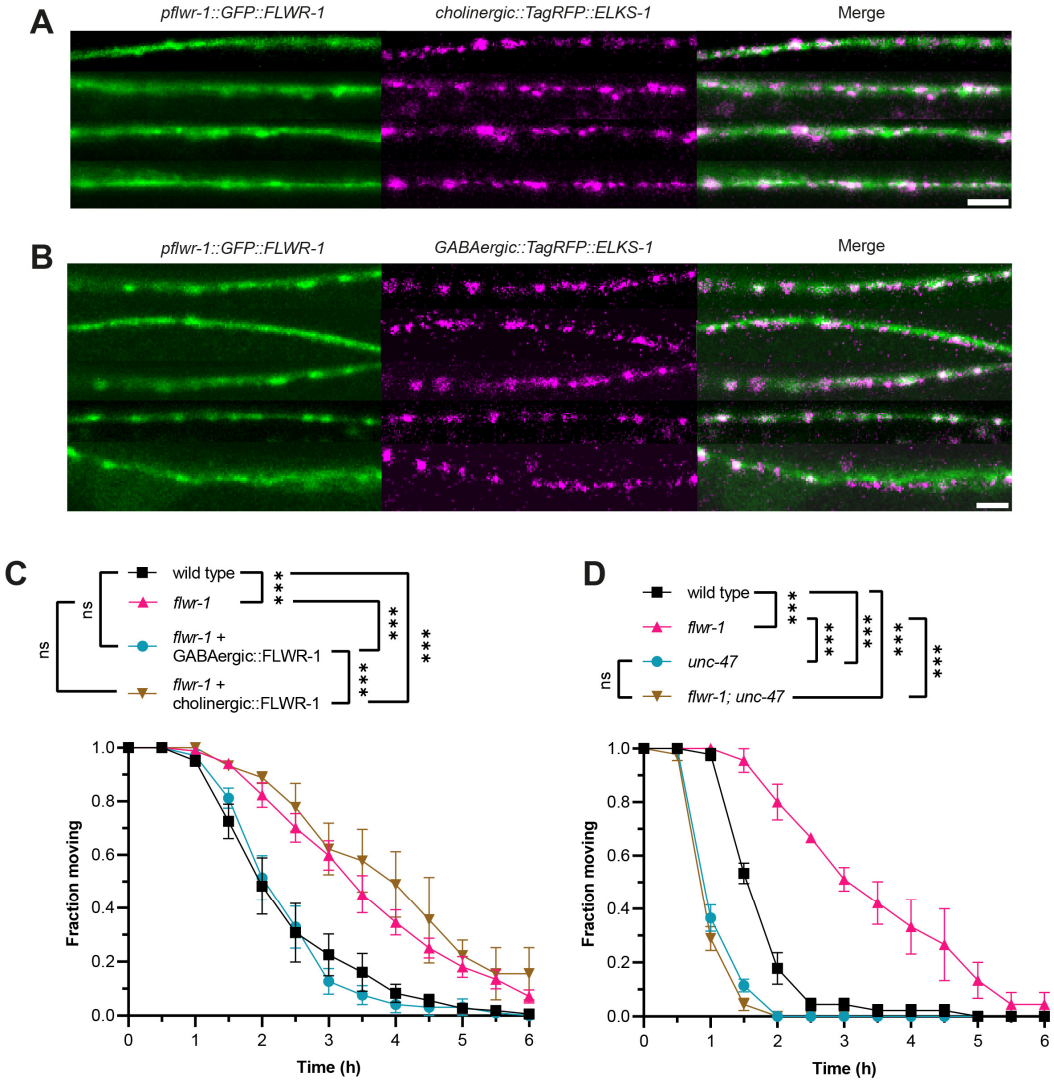

Fig. 3. GABAergic signaling is increased in *flwr-1* knockout mutants.

(A) Representative confocal micrographs of the DNCs in animals co-expressing *pflwr-1::GFP::FLWR-1* and *TagRFP::ELKS-1* in cholinergic motor neurons (*unc-17(short)* promoter). Scale bar, 5 µm. **(B)** Representative confocal micrographs of the DNCs in animals co-expressing *pflwr-1::GFP::FLWR-1* and *TagRFP::ELKS-1* in GABAergic neurons (*unc-47* promoter). Scale bar, 5 µm. **(C)** Mean (± SEM) fraction of moving animals after exposure to 1.5 mM aldicarb with cholinergic (*punc-17*) and GABAergic (*punc-47*) expression of FLWR-1 in *flwr-1(ok3128)* mutant background. N = 3 - 8 biological replicates. **(D)** Mean (± SEM) fraction of moving animals after exposure to 1.5 mM aldicarb with *unc-47(e307)* and *unc-47(e407)/flwr-1(ok3128)* double mutants. N = 3 biological replicates. **(C + D)** Two-way ANOVA with Tukey's correction. ns not significant, *** $p < 0.001$.

393 Yet, we also observed enrichment of FLWR-1 in fluorescent puncta indicating presynaptic localization (**Fig. 3A,**
394 **B**). Moreover, FLWR-1 partially colocalized with the dense projection marker ELKS-1 in cholinergic as well as in
395 GABAergic neurons (**Fig. 3A, B**; **Fig. S3C-E**; Dai et al. (2006); Kittelmann et al. (2013a)). Unlike ELKS-1, FLWR-
396 1 could also be found to a lesser extent in intersynaptic regions. This indicates that FLWR-1 might be involved in
397 neurotransmission at both cholinergic and GABAergic NMJs yet is not exclusively localized to active zones. To
398 determine whether the site of action of FLWR-1 in NMJ signaling is evenly located to cholinergic and GABAergic
399 neurons, we rescued FLWR-1 in each subset of these neurons. To achieve the intended expression, the promoters of
400 the vesicular transporters of acetylcholine (UNC-17) and GABA (UNC-47) were inserted in front of the FLWR-1
401 genomic sequence. Surprisingly, expression of FLWR-1 in GABAergic, but not in cholinergic, neurons rescued
402 aldicarb resistance (**Fig. 3C**). This was unexpected since mutations affecting SV recycling commonly lead to a
403 slowed replenishment of SVs and thus reduced acetylcholine release (Salcini et al., 2001; Schuske et al., 2003; Yu
404 et al., 2018). However, our results indicate that loss of FLWR-1 leads to increased release of GABA which
405 counteracts the aldicarb induced paralysis (Camara et al., 2019). To confirm this, we crossed *flwr-1* mutants into
406 animals which lack the vesicular GABA transporter UNC-47. This abolishes GABA release and induces
407 hypersensitivity to aldicarb (Vashlishan et al., 2008). We observed that the additional mutation of *unc-47* led to a
408 complete loss of aldicarb resistance in *flwr-1* mutants (**Fig. 3D**). This supports the notion that increased GABA
409 signaling, not decreased acetylcholine release, is the main cause of aldicarb resistance in *flwr*-1 animals.

410 **Neuronal excitability is increased in *flwr-1* mutants.**

411 Since the release of GABA appeared to be increased in *flwr-1* mutant animals, we wondered whether the excitability
412 of GABAergic neurons is increased. To test this, the fluorescent Ca^{2+} indicator GCaMP was expressed in
413 GABAergic neurons, allowing us to estimate relative Ca^{2+} levels at presynaptic sites (Nakai et al., 2001; Lu et al.,
414 2022). We co-expressed the red-shifted ChrimsonSA channelrhodopsin variant to control depolarization of neurons,
415 independent of GCaMP excitation light (Oda et al., 2018; Seidenthal et al., 2022). As expected, optogenetic
416 stimulation caused an increase in GCaMP fluorescence at NMJs in the DNC (**Fig. 4A**). Comparing wild type and
417 *flwr-1* mutants, we found that the gain in fluorescence intensity was significantly higher in animals lacking FLWR-
418 1 (**Fig. 4A, B**), supporting our previous finding of increased neurotransmission in GABAergic neurons. To verify
419 this at the behavioral level, we used a strain expressing ChR2(H134R) in GABAergic neurons, as it can be used to
420 assess GABA release through measurement of body length (Liewald et al., 2008). Since GABA receptors
421 hyperpolarize muscle cells, optogenetic stimulation of GABAergic motor neurons causes relaxation and thus
422 increased body length (Schultheis et al., 2011; Seidenthal et al., 2022). To augment the effect of ChR2 stimulation
423 on body length and to observe the effect of GABA release independent of cholinergic neurotransmission, the assay
424 was performed in a mutant background lacking a functional subunit of the levamisole receptor (*unc-29*; Fleming et
425 al. (1997); Richmond and Jorgensen (1999)). As expected, stimulation with blue light led to increased body length
426 (**Fig. 4C**). In accordance with Ca^{2+} imaging results, *flwr-1; unc-29* double mutants showed a significantly stronger
427 elongation during stimulation compared to the *unc-29* single mutant (**Fig. 4C, D**). These results indicate that Ca^{2+}
428 influx into the synapse is increased, likely causing more GABA to be released in animals lacking FLWR-1. The
429 previously observed aldicarb resistance indicates that this change in GABAergic transmission outweighs possible
430 changes in cholinergic transmission (**Fig. 3**). To investigate whether neuronal excitability may be generally
431 upregulated in *flwr-1* mutants, we assessed whether Ca^{2+} influx is affected in cholinergic motor neurons as well (**Fig.**
432 **4E, F**). Again, we observed increased GCaMP fluorescence levels during optogenetic stimulation. Together, these
433 results indicate that loss of FLWR-1 conveys an upregulation of neuronal excitability during continuous stimulation
434 in both classes of motor neurons (**Fig. 4G**). However, the overall E/I balance appears to be shifted towards stronger
435 inhibition of BWMs.

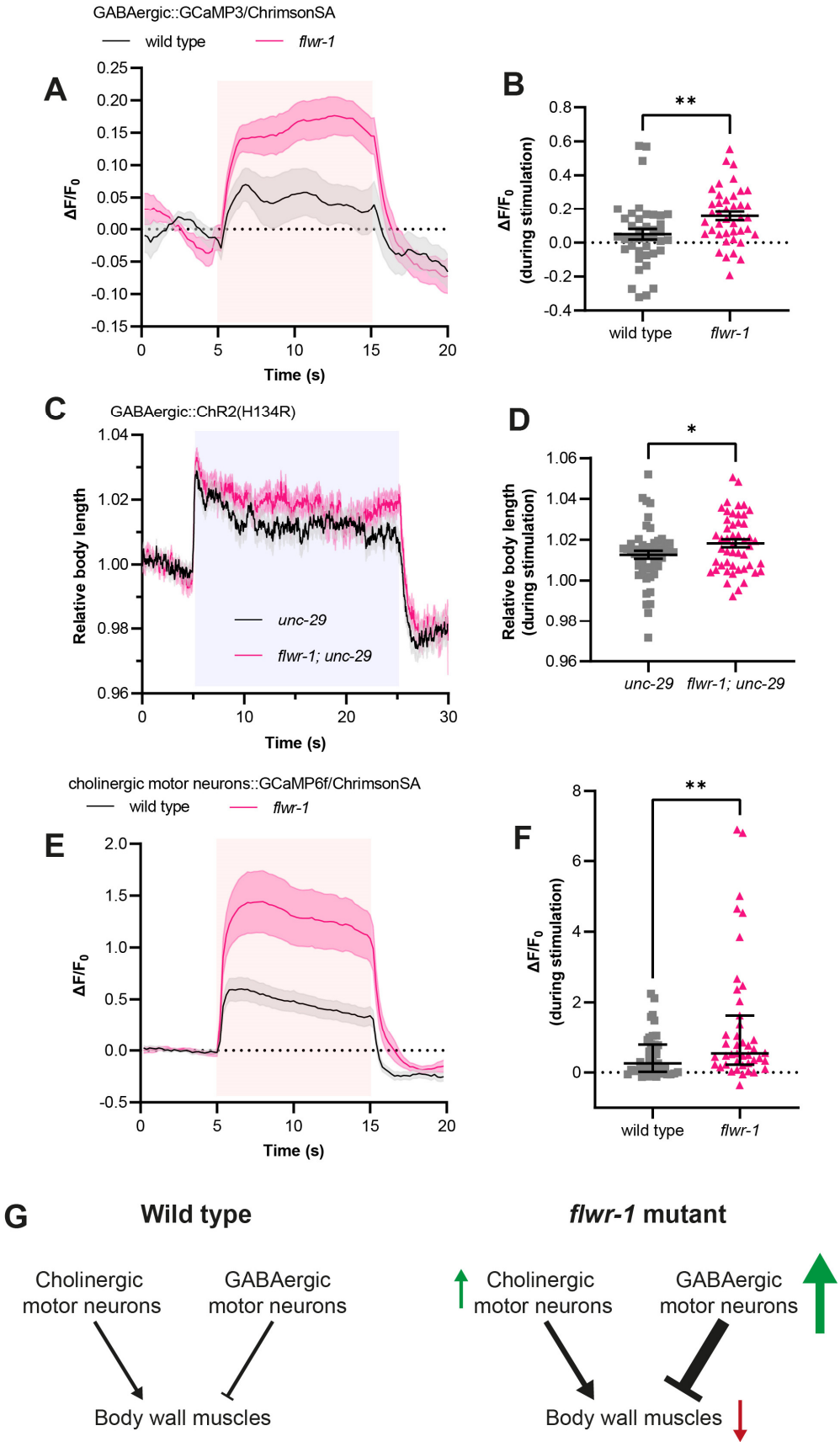

Fig. 4. Loss of FLWR-1 induces increased neuronal excitability.

(A) Mean (± SEM) normalized DNC fluorescence of animals expressing GCaMP3 and ChrimsonSA in GABAergic neurons (*unc-25* promoter). All animals were supplemented with ATR. A 10 s light pulse (590 nm, 40 µW/mm^2) was applied after 5 s as indicated by red shade. **(B)** Mean (± SEM) normalized fluorescence during stimulation (seconds 6 to 14) as depicted in (A). Each dot indicates a single animal. Unpaired t-test. ** $p < 0.01$. **(A + B)** Number of animals imaged in N = 5 biological replicates: wild type = 40, *flwr-1* = 41. Outliers were removed from both datasets as detected by the iterative Grubb's method (GraphPad Prism). **(C)** Mean (± SEM) body length of animals expressing ChR2(H134R) in GABAergic neurons (*unc-47* promoter) in the *unc-29(e1072)* mutant background, normalized to the average before stimulation. All animals were supplemented with ATR. A 20 s light pulse (470 nm, 100 µW/mm^2) was applied after 5 s as indicated by blue shade. **(D)** Mean (± SEM) relative body length during stimulation (seconds 6 to 24) as depicted in (C). Each dot indicates a single animal. Unpaired t-test. * $p < 0.05$. Number of animals measured in N = 4 biological replicates: wild type = 51, *flwr-1* = 49. **(E)** Mean (± SEM) normalized DNC fluorescence of animals expressing GCaMP6f and ChrimsonSA in cholinergic motor neurons (*unc-17b* promoter). All animals were supplemented with ATR. A 10 s light pulse (590 nm, 40 µW/mm^2) was applied after 5 s as indicated by red shade. **(F)** Median (with IQR) normalized fluorescence during stimulation (seconds 6 to 14) as depicted in (E). Each dot indicates a single animal. Mann-Whitney test. ** $p < 0.01$. **(E + F)** Number of animals imaged in N = 6 biological replicates: wild type = 41, *flwr-1* = 43. Outliers were removed from both datasets as in (B). **(G)** Schematic representation of motor neuron innervation of BWMs. Arrows indicate putative increased (green) or decreased (red) neurotransmission/excitation of the involved cell types in *flwr-1* mutants compared to wildtype.

Endocytosis is slowed in *flwr-1* mutants in non-neuronal cells and neurons.

Homologues of FLWR-1 were found to be involved in endocytosis in neuronal as well as non-neuronal cells (Yao et al., 2009; Chang et al., 2018; Rudd et al., 2023). We thus wondered whether this function is evolutionarily conserved in nematodes. One possibility to assess this in *C. elegans* is to observe the efficiency of endocytosis by coelomocytes (Fares and Greenwald, 2001). These scavenger cells continuously endocytose fluid from the body cavity and loss of endocytosis-associated factors leads to a defective uptake of proteins secreted from other tissues (Fares and Grant, 2002). By expressing GFP fused to a secretory signal sequence which is discharged from BWMs, endocytic uptake by coelomocytes can be quantified by fluorescence microscopy (Fares and Greenwald, 2001; Bednarek et al., 2007). According to single-cell RNAseq data, FLWR-1 is expressed in coelomocytes (**Supplementary Table 3**; Taylor et al. (2021)). Indeed, mutation of *flwr-1* led to strongly reduced GFP fluorescence levels within coelomocytes indicating a reduced uptake by endocytosis (**Fig. 5A, B**).

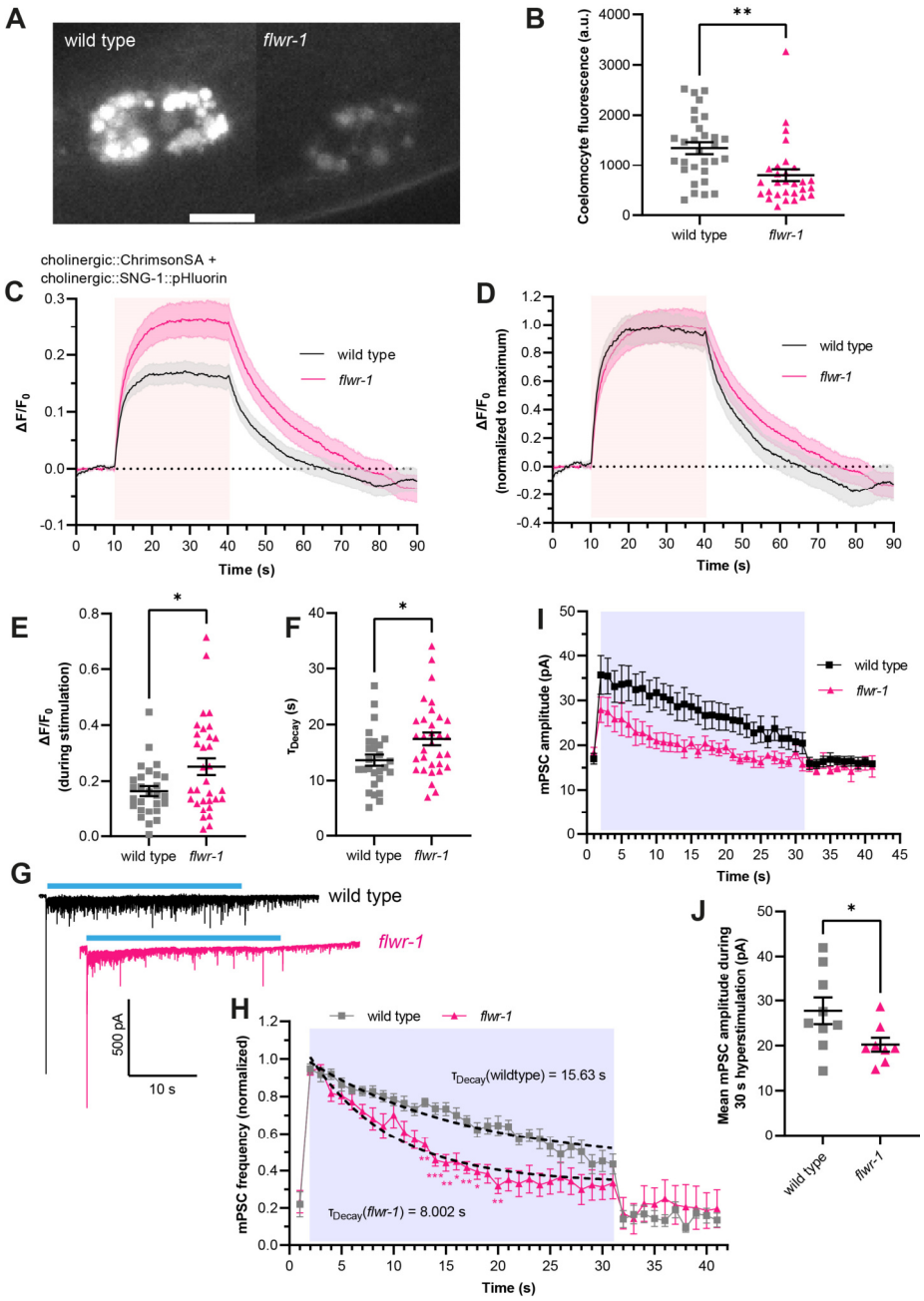

Fig. 5. FLWR-1 facilitates endocytosis in non-neuronal and neuronal cells.

(A) Exemplary images of coelomocytes in wild type and *flwr-1(ok3128)* animals expressing secreted ssGFP in BWMs (*myo-3* promoter). Scale bar, 10 µm. **(B)** Mean (± SEM) background corrected fluorescence of coelomocytes. Each dot indicates the mean coelomocyte fluorescence per animal. a.u. = arbitrary units of fluorescence intensity. Mann-Whitney test. *** $p < 0.001$. Number of animals imaged in N = 3 biological replicates: wild type = 30, *flwr-1* = 29. **(C)** Mean (± SEM) normalized DNC fluorescence of animals expressing SNG-1::pHluorin and ChrimsonSA in cholinergic neurons (*unc-17* promoter). All animals were supplemented with ATR. A 30 s light pulse (590 nm, 40 µW/mm^2) was applied after 10 s as indicated by the red shade. **(D)** Mean (± SEM) pHluorin fluorescence as depicted in (C) but additionally normalized to the maximum value of each dataset. **(E)** Mean (± SEM) normalized fluorescence during stimulation (seconds 15 to 35) as depicted in (C). Each dot indicates a single animal. Unpaired t-test. **(F)** Mean (± SEM) calculated exponential decay constants of fluorescence decline after stimulation. Each dot indicates a single animal. Unpaired t-test. **(C – F)** Number of animals imaged in N = 5 biological replicates: wild type = 27, *flwr-1* = 32. * $p < 0.05$. **(G)** Representative voltage-clamp recordings of currents detected in BWMs. Animals express ChR2(H134R) in cholinergic motor neurons (*unc-17* promoter, transgene *zxIs6*) and have been treated with ATR. A 30 s light stimulus (470 nm, 8 mW/mm^2) was applied as indicated by blue bars. **(H)** Normalized mPSC frequency in BWMs. All animals were treated with ATR. A 30 s light pulse (470 nm, 8 mW/mm^2) was applied as indicated by blue shade. Dashed lines indicate one-phase exponential regression

547 analysis fitted to the mean mPSC frequencies during stimulation. Calculated time constants of decay are shown. Two-way ANOVA with
548 Šidák's correction. All significant differences to wild type are depicted. **(I)** mPSC amplitude in BWMs of animals measured in (G + H).
549 **(J)** Mean (± SEM) mPSC amplitude during light stimulation as indicated in (I). Unpaired t-test. * $p < 0.05$. (G - J) Number of animals:
550 wild type = 9, *flwr-1* = 8.

551 We further used the recently established pOpsicle (pH-sensitive optogenetic reporter of synaptic vesicle recycling)
552 assay to estimate the amount of SV fusion and the rate of recycling of SV components in cholinergic neurons
553 (Seidenthal et al., 2023). This assay combines a pHluorin based probe fused to an SV-associated protein (SNG-1)
554 and optogenetic stimulation of neurotransmitter release; this way, pHluorin fluorescence is unquenched during
555 stimulated exocytosis and quenched during SV endocytosis and recycling (Sankaranarayanan et al., 2000). Loss of
556 FLWR-1 led to significantly increased fluorescence signals during stimulation which indicates more SV fusion
557 compared to wild type (**Fig. 5C, E**). This is in accordance with the increased excitability of cholinergic neurons we
558 observed earlier (**Fig. 4E, F**). Moreover, the rate of fluorescence decay after stimulation was significantly delayed
559 in *flwr-1* mutants suggesting slower recycling of SVs, or reduced acidification of endosomal structures or SVs after
560 recycling (**Fig. 5D, F**).

561 Slowed replenishment of SV pools caused by defective recycling is known to cause synaptic depression, as assessed
562 by electrophysiological measurements of post-synaptic currents (Wu and Betz, 1998; Kittelmann et al., 2013b; Krick
563 et al., 2021). This is also the case in *Drosophila* for animals lacking Flower (Yao et al., 2009). To address this in *C.*
564 *elegans*, we measured miniature post-synaptic currents (mPSCs) in BWMs, which reflect the post-synaptic effects
565 of presynaptic neurotransmitter release (Liewald et al., 2008; Weissenberger et al., 2011). Animals lacking FLWR-
566 1 showed no significant difference in unstimulated mPSC frequency or amplitude (**Fig. S4A, B**) which is in
567 accordance with FLWR-1 being dispensable in basal swimming locomotion (**Fig. 1C, D**). Similarly, pulsed
568 optogenetic stimulation of cholinergic neurons at different frequencies did not reveal a difference in the measured
569 currents between wild type and mutants (**Fig. S4C, D**) suggesting that FLWR-1 might be needed only during
570 continuous stimulation. Indeed, *flwr-1* mutants showed an accelerated rundown of the mPSC frequency in BWMs
571 during constant illumination (**Fig. 5G, H**). This is in accordance with a role of FLWR-1 in SV recycling.
572 Surprisingly, mPSC amplitudes in *flwr-1* mutants are reduced during 30 s hyperstimulation (**Fig. 5I, J**). This suggests
573 that either the amount of neurotransmitter released from a single SV or the number of multivesicular fusion events
574 is decreased (Liu et al., 2005). The absolute mPSC frequency, which represents the number of SVs fusing per time,
575 was also smaller during continuous stimulation in *flwr-1* animals (**Fig. S4E, F, G**). These results contrast the
576 increased excitability of cholinergic neurons we observed (**Fig. 4A, E**). Since cholinergic neurons also stimulate
577 GABAergic neurons, and since GABAergic minis are also evaluated here, the dissection of animals, required for
578 electrophysiological recordings, could damage neuronal commissures, causing an interruption of physiological
579 signal transmission, which is otherwise observed in intact animals. We further analyzed whether *flwr-1* mutants can
580 recover from strong optogenetic 30 s stimulation by applying a short stimulus after a recovery period (inter stimulus
581 interval, ISI) of 15 s, and found no significant difference to wildtype (**Fig. S4E, H**). This suggests that a 15 s ISI is
582 sufficient for *flwr-1* mutants to recover to the same extent as wild type synapses. In sum, our results support a
583 facilitatory role of FLWR-1 in SV recycling specifically during continuous stimulation.

584 **Loss of FLWR-1 leads to depleted SV pools and accumulation of endosomal structures after optogenetic**
585 **stimulation.**

586 Mutations which affect endocytosis commonly have fewer SVs because of defective recovery of SV components
587 which could also be shown for Flower defective *Drosophila* boutons (Schuske et al., 2003; Yao et al., 2009). Such
588 a defect is even more pronounced when samples are conserved immediately following optogenetic stimulation by
589 high-pressure freezing (Kittelmann et al., 2013b; Yu et al., 2018). In nematodes, this optogenetic stimulation can be
590 controlled by supplementing all-*trans* retinal (ATR), the chromophore of ChR2 (Nagel et al., 2005). Ultrastructural
591 analysis using transmission electron microscopy (TEM) indeed revealed fewer SVs in stimulated *flwr-1* mutant
592 synapses compared to wild type (**Fig. 6A, B**). This indicates that *flwr-1* mutants, unlike wild type, are unable to refill
593 SV pools sufficiently fast. At the same time, loss of *Drosophila* Flower has been shown to cause defective formation

of bulk endosomal structures after strong stimulation (Yao et al., 2017). In contrast to this, we observed an increased, rather than decreased, number of endosomes in stimulated *flwr-1* mutant synapses (**Fig. 6C**). This may either be caused by increased SV fusion which triggers bulk endosomal formation (Clayton et al., 2008; Wu et al., 2014) or defective breakdown of recycling endosomes (Watanabe et al., 2013; Gan and Watanabe, 2018; Yu et al., 2018). Our pHluorin imaging data (**Fig. 5C - F**), would support the notion that both, increased SV fusion as well as defective recovery and subsequent acidification of SVs, may cause the higher number of endosomes in *flwr-1* mutants. However, we note that our stimulation regime likely resembles a more physiological activation of neurotransmission compared to the intense stimuli previously used (Yao et al., 2017), as wild type synapses only rarely contained endosomal structures. Moreover, we observed fewer docked vesicles in *flwr-1* animals which have been treated with ATR, compared to those without (**Fig. 6D**). This might be caused by increased SV fusion and is in line with the increased excitability we observed before. The number of large vesicles and neuropeptide-containing dense core vesicles (DCVs) is unchanged in animals lacking FLWR-1 (**Fig. S5**).

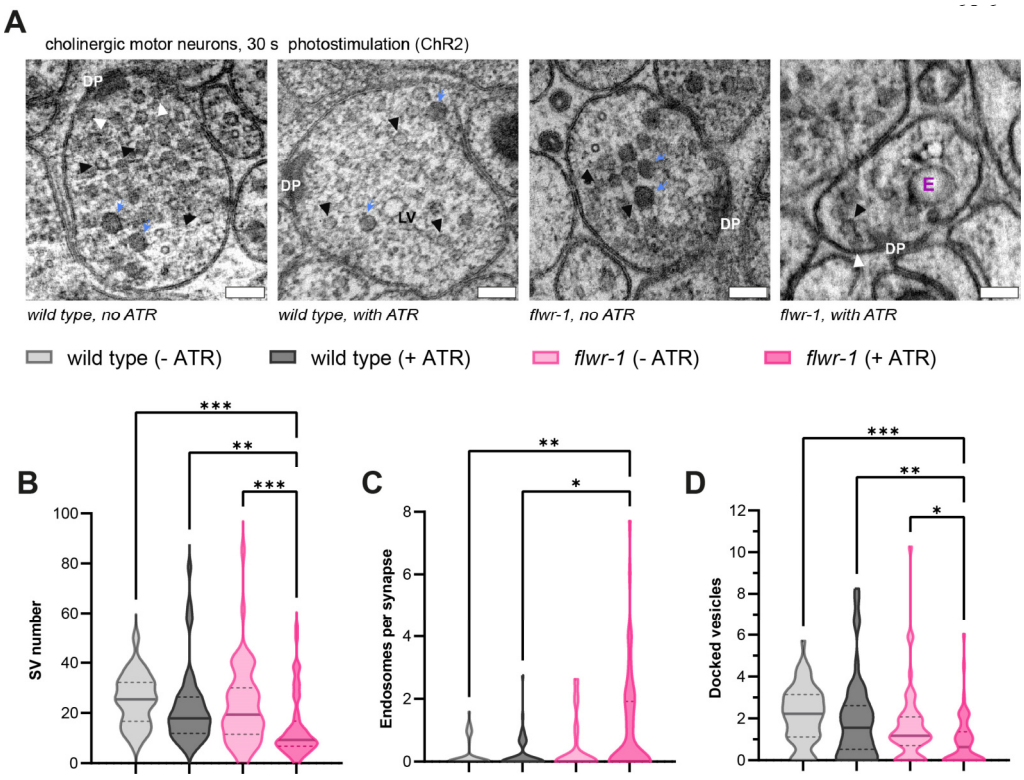

Fig. 6. Ultra-structural analysis reveals defective recycling of SVs after stimulation in *flwr-1* mutants.

(A) Representative TEM micrographs of cholinergic *en-passant* synapses in wild type and *flwr-1(ok3128)* animals expressing ChR2(H134R) in cholinergic motor neurons (*unc-17* promoter). Animals were optionally treated with ATR as indicated. Dense projections (DP), endosomes (E), dense core vesicles (blue arrows), SVs (black arrowheads), docked vesicles (white arrowheads) and large vesicles (LV) are indicated. Scale bars, 100 nm. **(B)** Violin plot depicting the number of SVs counted per synaptic profile. **(C)** Violin plot depicting the number of docked vesicles observed per synaptic profile. **(D)** Violin plot depicting the number of endosomes per synapse. **(B - D)** Bold line represents the median, and the dashed lines the IQR. Kruskal-Wallis test. Only statistically significant differences are depicted. * $p < 0.05$,** $p < 0.01$, *** $p < 0.001$. Number of synaptic profiles imaged: wild type (-ATR) = 56, wild type (-ATR) = 51, *flwr-1* (-ATR) = 55, *flwr-1* (+ATR) = 59.

The increased excitability of *flwr-1* neurons may be caused by deregulation of MCA-3.

While a facilitatory role of Flower in endocytosis appears to be conserved in *C. elegans*, we found no evidence that FLWR-1 conducts Ca^{2+} upon insertion into the PM (Yao et al., 2009). On the contrary, Ca^{2+} levels are increased during strong stimulation of neurons in animals lacking FLWR-1. We thus wondered whether clearance of Ca^{2+} which has entered the synapse via VGCCs, might be defective in *flwr-1* mutants. In neurons and muscles, the plasma membrane Ca^{2+} ATPase (PMCA) is involved in extruding Ca^{2+} from the cell (Boczek et al., 2019; Krick et al., 2021; Krebs, 2022). The *C. elegans* homolog MCA-3 (also known as CUP-7) is expressed in neurons, muscle cells and coelomocytes (**Fig. S6**, **Supplementary Table 3**; Bednarek et al. (2007); Taylor et al. (2021)). Interestingly, reducing the function of MCA-3 by mutation was shown to cause a similar defect in endocytosis of secreted GFP in coelomocytes as the loss of FLWR-1 does (**Fig. 5A, B**; Bednarek et al. (2007)). We therefore wondered whether MCA-3 might be negatively affected in *flwr-1* mutants. To assess this, we used a mutant (*ok2048*) lacking part of

the C-terminus of MCA-3 including part of the regulatory calmodulin-binding domain (Kraev et al., 1999; Consortium, 2012; Mantilla et al., 2023) (**Fig. 7A**).

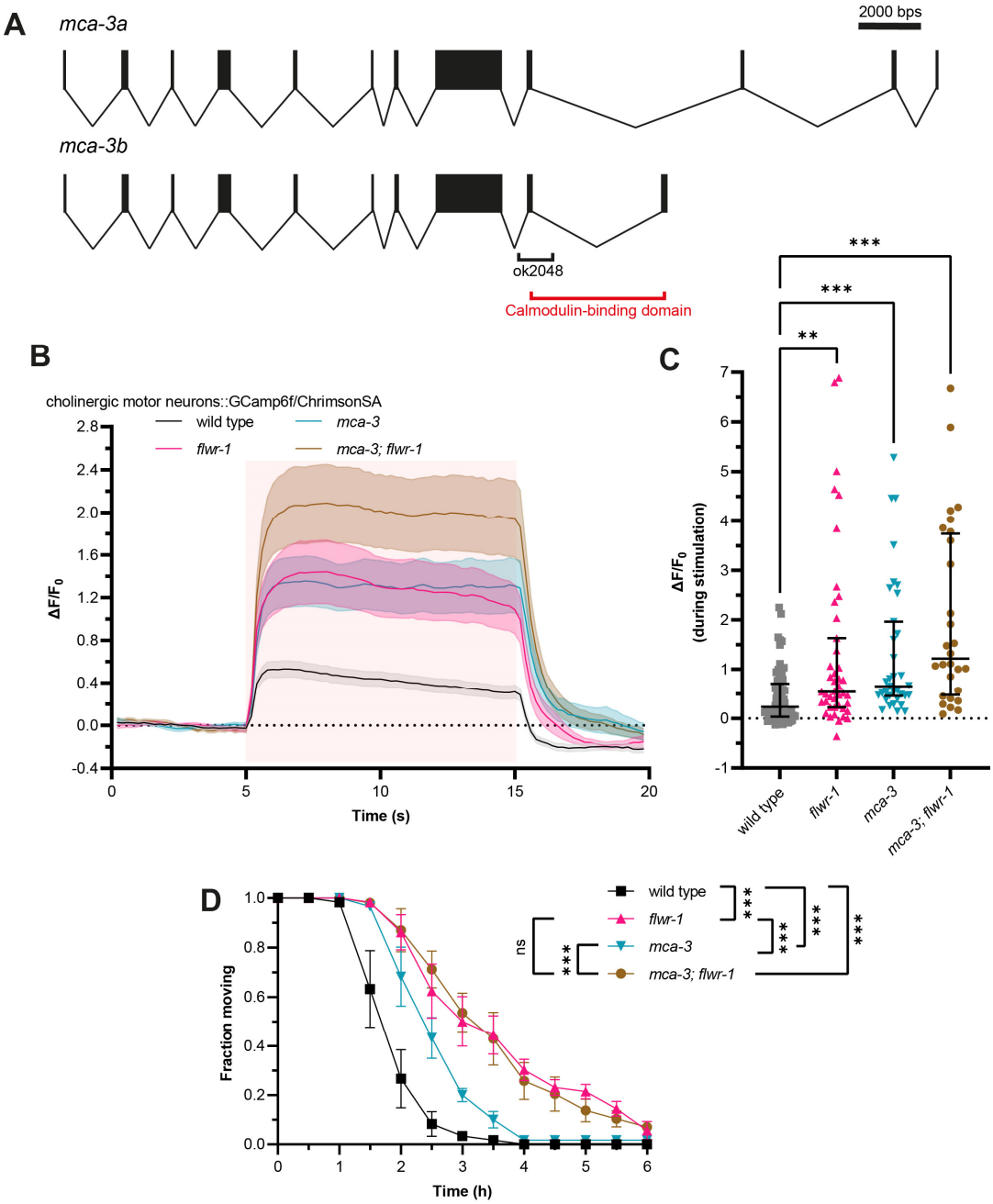

Fig. 7. Increased excitability in *flwr-1* mutants may be caused by negative regulation of MCA-3.

(A) Schematic representation of the *mca-3* gene locus including exon structure of isoforms *mca-3a* and *mca-3b*. Bars represent exons and connecting lines introns. The size of the *ok2048* deletion as well as the putative calmodulin-binding domain are indicated. **(B)** Mean (± SEM) normalized DNC fluorescence of animals expressing GCaMP6f and ChrimsonSA in cholinergic motor neurons (*unc-17b* promoter). All animals were supplemented with ATR. A 10 s light pulse (590 nm, 40 µW/mm^2) was applied after 5 s as indicated by red shade. **(C)** Median (with IQR) normalized fluorescence during stimulation (seconds 6 to 14) as depicted in (B). Each dot indicates a single animal. Kruskall-Wallis test. Only statistically significant differences are depicted. ** $p < 0.01$, *** $p < 0.001$. **(B + C)** Number of animals imaged: wild type = 65, *flwr-1* = 43, *mca-3* = 35, *mca-3; flwr-1* = 28. Outliers were removed from all datasets as detected by iterative Grubb's method (GraphPad Prism). **(D)** Mean (± SEM) fraction of moving animals after exposure to 1.5 mM aldicarb. Two-way ANOVA with Tukey's correction. ns not significant, *** $p < 0.001$.

Since full knockouts of *mca-3* are lethal, it is likely that this represents a reduction-of-function mutation (Bednarek et al., 2007). As expected, *mca-3* mutants displayed increased Ca^{2+} influx (or net Ca^{2+} levels, representing the summed VGCC-mediated entry and MCA-3-mediated efflux) upon optogenetic stimulation of cholinergic motor neurons (**Fig. 7B, C**). Elevated Ca^{2+} levels appeared to be further enhanced by additionally mutating *flwr-1*, however this did not meet significance. This was likely due to the large variance in the measurements, which was due to some cells showing very low basal Ca^{2+} levels (i.e. GCaMP fluorescence) yet reaching similarly high levels during stimulation. As is, our data suggest that the two genes are not in a common pathway, as the effects appear to be additive. However, the *mca-3* mutant used here is only a reduction-of-function mutant, thus additional deregulation by loss of FLWR-1 may explain the possible additive effect. A different picture was observed in aldicarb assays: Reduction of MCA-3 function conveyed aldicarb resistance that was, however, less pronounced than for *flwr-1*

mutants (**Fig. 7D**). Here, the double mutant did not further augment the mutant phenotype of *flwr-1*, which may be interpreted as that both proteins function in the same pathway, where *flwr-1* is upstream of *mca-3*.

FLWR-1 structure prediction does not imply Ca^{2+} conducting ability but $PI(4,5)P_2$ binding.

We observed increased rather than decreased Ca^{2+} influx during stimulation, which contrasts findings from *D. melanogaster* Flower (Yao et al., 2017). Previously, an evolutionarily conserved glutamate residue within the transmembrane domain has been proposed to be a Ca^{2+} selectivity filter because of similarities to $Ca_v1.2$ and TRP channels (Yao et al., 2009). This group therefore proposed that Flower, like TRP channels, can form homo-tetramers to conduct Ca^{2+} (Hoenderop et al., 2003; Yao et al., 2009; Zhang et al., 2023). We therefore wondered whether loss of the conserved glutamate residue impacts FLWR-1 function in *C. elegans* (**Fig. 8A**). Surprisingly, expressing a mutant variant of FLWR-1 in which glutamate 74 is exchanged to glutamine significantly decreased the aldicarb resistance of the *flwr-1* mutant (**Fig. 8B**). This suggests that the respective glutamate may not be essential for FLWR-1 function but may have an impact on protein stability. We thus performed structure and oligomerization prediction of FLWR-1 using Alphafold 3 (AF3) to estimate the approximate location of the conserved glutamate residue within a putative FLWR-1 homotetramer (Evans et al., 2022; Abramson et al., 2024). One of the predicted complexes indeed revealed a pore-like structure (**Fig. S7A**). However, while conventional Ca^{2+} conducting channels contain a glutamate residue within their pore domain (Chen et al., 2023) (**Fig. S7B**), E74 of FLWR-1 is not part of pore-lining residues in the predicted tetramer.

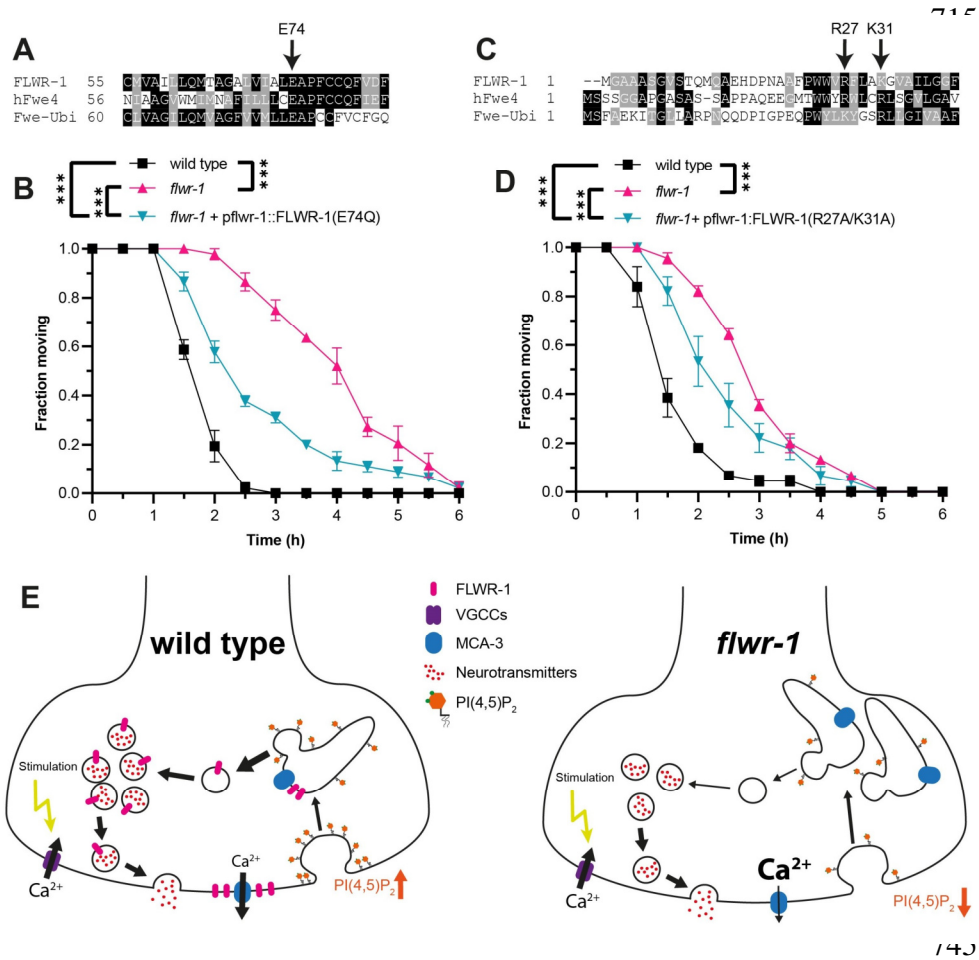

Fig. 8. Basic amino acid residues on the intracellular surface of FLWR-1 may be involved in $PI(4,5)P_2$ lipid binding.

(**A**) Partial alignment of the amino acid sequences of FLWR-1, hFwe4 (*Homo sapiens*), and Fwe-Ubi (*Drosophila melanogaster*). Shading depicts evolutionary conservation of amino acid residues (black – identity; grey - homology). (**B**) Mean (± SEM) fraction of moving animals after exposure to 1.5 mM aldicarb. A mutated FLWR-1 in which glutamate 74 was changed to glutamine was expressed in *flwr-1(ok3128)* mutant background under its endogenous promoter. Two-way ANOVA with Tukey's correction. N = 3 biological replicates. *** $p < 0.001$. (**C**) As in (A), highlighting the N-terminal sequences. (**D**) Mean (± SEM) fraction of moving animals after exposure to 1.5 mM aldicarb. A mutated FLWR-1 in which arginine 27 and lysine 31 were altered to alanines, was expressed in *flwr-1(ok3128)* mutant background under its endogenous promoter. Two-way ANOVA with Tukey's correction. N = 3 biological replicates. (**E**) Model summarizing findings made in this study. For details, see discussion.

748 FLWR-1, like MCA-3, has further been suggested to bind to phosphatidylinositol-4,5-bisphosphate (PI(4,5)P_2), an
749 important regulator of SV recycling, and affect its levels within the PM (Bednarek et al., 2007; Lopreiato et al.,
750 2014; Li et al., 2020). Binding of transmembrane proteins (including TRP channels) to PI(4,5)P_2 is generally
751 mediated by positively charged amino acid residues (lysine and arginine) close to the intracellular side of the PM,
752 which bind to the negatively charged phosphate residues (**Fig. S7C**) (Ribalet et al., 2005; Hansen et al., 2011;
753 Duncan et al., 2020; Rohacs, 2024). The predicted FLWR-1 structure similarly contains many basic amino acids
754 which are likely to be close to the intracellular PM leaflet (**Fig. S7D**). *In silico* docking prediction was then used to
755 estimate how PI(4,5)P_2 may bind to FLWR-1. In the resulting structure, both phosphate residues are close to lysine
756 31 and arginine 27 (**Fig. S7D**). A positive charge at this position is evolutionarily conserved, suggesting an important
757 function (**Fig. 8C**). Moreover, these amino acids have been suggested to mediate PI(4,5)P_2 binding in *D.*
758 *melanogaster* Flower (Li et al., 2020). Expression of a mutated version of FLWR-1 in which both residues were
759 replaced by alanines only partially rescued aldicarb resistance (**Fig. 8D**), implying that FLWR-1 function may be
760 facilitated by these residues and their potential interaction with PI(4,5)P_2.

761 These findings implicate that the conserved glutamate residue 74 is not essential, yet still important for FLWR-1
762 activity. In addition, an interaction with PI(4,5)P_2 *via* basic amino acids also seems to be an important factor.
763 However, we do note that FLWR-1 structural models as depicted here rely on *in silico* predictions. The actual
764 biological structure of FLWR-1, or its homologues, has yet to be determined using X-ray crystallography or cryo-
765 EM.

766 Discussion

767 Here, we found that loss of FLWR-1 conveyed increased excitability of motor neurons, particularly GABAergic
768 neurons, thus leading to more GABA release. This gives rise to an E/I imbalance at the NMJ. We showed that
769 FLWR-1 is localized to SVs in neuronal cells, and we found an accumulation of endosomal structures as well as
770 slowed acidification kinetics in *flwr-1* mutant animals, suggesting defective recovery of SVs from recycling
771 endosomes. We further found indications that deregulation of PMCAs may be the cause of the increased excitability
772 of *flwr-1* neurons (see model, **Fig. 8E**).

773 MCA-3 has previously been suggested to facilitate endocytosis in other cells, namely coelomocytes (Bednarek et
774 al., 2007). This indicates that both, increased excitability as well as defective endocytosis in coelomocytes, may be
775 influenced by deregulation of MCA-3 in *flwr-1* mutants. Whether FLWR-1 directly activates expression or function
776 of MCA-3, or whether this is caused by a homeostatic change because of the loss of FLWR-1, is yet unclear.
777 However, it is important to note that *Drosophila* Flower was shown to increase neuronal PI(4,5)P_2 levels, which
778 drives ADBE during sustained neurotransmission (Li et al., 2020). We could show that an involvement with
779 PI(4,5)P_2 is likely conserved in nematodes. Similarly, MCA-3 was important to maintain PI(4,5)P_2 in coelomocytes
780 (Bednarek et al., 2007). Thus, FLWR-1 and MCA-3 may have a shared role in the regulation of PI(4,5)P_2 levels.
781 The question thus arises, whether FLWR-1 acts upstream of MCA-3 or vice versa or whether they act in parallel.
782 Our results indicate that MCA-3 may be functionally affected in *flwr-1* mutants explaining increased Ca^{2+} levels
783 during stimulation (Brini and Carafoli, 2011; Chamberland et al., 2019). Alternatively, MCA-3 may undergo endo-
784 exocytosis and this could be affected by effects of the *flwr-1* mutation on endocytosis and recycling (Ono et al.,
785 2019). The increased Ca^{2+} influx we observed was at first surprising, since work in *Drosophila* has yielded opposite
786 results during 40 Hz electrical stimulation in neuromuscular boutons of Flower mutants (Yao et al., 2017). At
787 stimulation with 10 Hz, however, these animals showed an increased GCaMP signal compared to wild type, in line
788 with our observations. Potentially, increased excitability is only observed with lower, more physiological stimulation
789 of neurons.

790 Even though we observed increased, instead of decreased, Ca^{2+} influx into the pre-synapse in *flwr-1* mutants, we
791 cannot conclude about the putative Ca^{2+}-conducting activity of FLWR-1. However, it was discussed that the kinetics
792 of Ca^{2+} influx induced by Flower in *Drosophila* are too slow and the extent too little as to directly trigger known
793 modes of endocytosis (Brose and Neher, 2009; Xue et al., 2012; Leitz and Kavalali, 2016). Therefore, rather than

794 having a function in directly coupling exo- and endocytosis, we suggest that FLWR-1 has a regulatory role in
795 facilitating SV recycling, potentially by affecting MCA-3 activity. Increased Ca^{2+} at endocytic sites could, for
796 example, lead to activation of the Ca^{2+} sensor calmodulin which has been shown to promote endocytosis in nerve
797 terminals (Wu et al., 2009). However, whether the small and slow Ca^{2+} influx observed for *Drosophila* Flower is
798 sufficient to activate calmodulin is unclear (Wu et al., 2009; Yao et al., 2009). To assess the possibility of FLWR-1
799 forming an ion channel, we used artificial intelligence-based protein structure prediction. Assuming similarity to
800 Ca^{2+} channels, we asked AF3 to model FLWR-1 as a tetramer. The putative pore lining residues were mostly
801 hydrophobic or apolar, thus not well in agreement with a function as an ion channel. The suggested similarity to the
802 selectivity filter of VGCCs, including the sequence EGW or EAW (in FLWR-1 this is EAP; Yao et al. (2009)) was
803 not confirmed in the AF3 models: While glutamate faces the extracellular end of the VGCC pore in all four channel
804 modules, $E74_{FLWR-1}$ pointed away from the pore. We thus think that FLWR-1 is very unlikely to form an ion channel.

805 Should FLWR-1 exert an influence on $PI(4,5)P_2$ levels, this may activate PMCAs (Berrocal et al., 2017), which
806 would remove Ca^{2+} and prevent sustained phospholipase C activity, thus protecting $PI(4,5)P_2$ at the PM from
807 hydrolysis (Lopreiato et al., 2014; Penniston et al., 2014). Increased $PI(4,5)P_2$ levels could then activate different
808 forms of endocytosis (Posor et al., 2015; Blumrich et al., 2023). Such interactions could further trigger a positive
809 feedback loop leading to invagination of the PM (Yao et al., 2017). Both, PMCAs and Flower, were suggested to
810 directly bind $PI(4,5)P_2$ with positively charged amino acid residues in areas close to their respective transmembrane
811 regions (Filoteo et al., 1992; Li et al., 2020). In line with this, the FLWR-1 AF3 model exhibits several amino acids
812 in positions that could interact with $PI(4,5)P_2$ headgroups in the membrane, similar to the interaction of potassium
813 channels with $PI(4,5)P_2$. This could lead to a close arrangement of both proteins in $PI(4,5)P_2$ lipid microdomains
814 (Katan and Cockcroft, 2020). Flower could also activate PMCAs in intracellular compartments after endocytosis.
815 One PMCA variant was shown to be mainly localized to recycling SVs and endosomes and Ca^{2+} influx into these is
816 an important factor in clearance from the presynapse (Ono et al., 2019). Overall, this may explain the increased
817 number of recycling endosomes found in *flwr-1* synapses. For example, effects of *flwr-1* mutations on $PI(4,5)P_2$ at
818 the PM may negatively affect bulk endocytosis. Yet effects on $PI(4,5)P_2$ at the endosome may have a stronger impact
819 in slowing down breakdown of these endosomes (**Fig. 8E**). Still, our ultrastructural analysis contrasts EM analyses
820 in *Drosophila* which yielded fewer, rather than more, bulk endosomal structures in animals lacking Flower (Yao et
821 al., 2017; Li et al., 2020). However, this group used an unusually long stimulation period of ten minutes which may
822 result in entirely different outcomes compared to our 30 s optogenetic stimulus. Alternatively, the subcellular
823 localization of Flower function may be different between organisms, since, in *C. elegans*, loss of FLWR-1 seems to
824 delay reformation of SVs from bulk endosomes.

825 Another possible explanation of how Flower could facilitate endocytosis was suggested by Yao et al. (2017),
826 proposing that calcineurin may function downstream of Flower to stimulate bulk endosome formation. Calcineurin
827 is a Ca^{2+}- and calmodulin-dependent phosphatase that activates endocytic proteins by dephosphorylation, thus
828 accelerating recycling of SVs (Cousin and Robinson, 2001; Kumashiro et al., 2005; Yamashita, 2012). The Ca^{2+}
829 increase, driving calcineurin, would result from effects of FLWR-1 on PMCAs in our model. But how do the
830 increased Ca^{2+} levels and the decreased rate of pHluorin decay we observe fit to this idea? One explanation could be
831 that more Ca^{2+} and thus more activation of calcineurin induces a shift of the main endocytic mode to ADBE
832 (Yamashita, 2012). Structures formed by bulk endocytosis are acidified more slowly than small SVs generated by
833 CME, which could explain the delayed decay of pHluorin fluorescence (Gross and von Gersdorff, 2016; Okamoto
834 et al., 2016). These observations are in line with the higher number of endosomal structures in *flwr-1* mutants that
835 we detected by EM. More pronounced neurotransmission, due to increased SV fusion, causes an increase in bulk
836 invaginations (Clayton et al., 2008), yet the endosomes formed this way are not efficiently disassembled. The *C.*
837 *elegans* homolog of calcineurin, TAX-6, is also involved in activity-dependent bulk endocytic processes, however
838 in a different context (Miller-Fleming et al., 2016; Cuentas-Condori et al., 2023). Here, this protein is rather required
839 for the regeneration of GABAergic synapses during maturation. Thus, the remote possibility that FLWR-1 also takes
840 part in this process needs to be considered, implying that developmental aspects of FLWR-1 function may influence

841 E/I balance even in adult NMJs. Jointly, these ideas suggest that calcineurin/TAX-6 could be upregulated, rather
842 than downregulated, by the increased Ca^{2+} levels during neurotransmission in *flwr-1* mutants.

843 In sum, our work confirms a conserved role of FLWR-1 in neurotransmission and SV recycling even though we
844 observed differences to previous data from *Drosophila* NMJs. We found an unexpected upregulation of
845 neurotransmission in *flwr-1* mutants which has not yet been observed in other animal models. Further investigation
846 will be required to confirm the involvement of MCA-3 and the nature of the relationship between these proteins.

847 Author Contributions

848 MS created plasmids. MS and NS generated strains. MS performed light microscopy, swimming assays,
849 pharmacological assays and body length measurements. SS conducted aldicarb assays. JR and DR prepared EM
850 samples and JR conducted EM experiments. JL performed electrophysiology. MS and AG designed and coordinated
851 the study. MS and AG wrote the manuscript. AG and SE supervised the work and acquired funding. All authors read
852 and approved the final manuscript.

853 Funding

854 This project was funded by Deutsche Forschungsgemeinschaft, Collaborative Research Centre 1080 project B02
855 (grant DFG CRC1080/B2 to AG), as well as by core funding from Goethe University.

856 Acknowledgments

857 We are indebted to Katharina Kuhlmeier for her expert technical assistance, and members of the Gottschalk group
858 for critical comments regarding the manuscript. We further thank Martina Rudgalvyte from the Glauser Lab
859 (Université de Fribourg) for helpful comments. We would also like to show our gratitude to members of the Zimmer
860 Lab (University of Vienna) for providing advice and plasmids for GCaMP imaging, and to the Wang Lab (University
861 of Connecticut) for providing plasmids. Some deletion mutations used in this work were provided by the
862 International *C. elegans* Gene Knockout Consortium (*C. elegans* Gene Knockout Facility at the Oklahoma Medical
863 Research Foundation, which is funded by the National Institutes of Health, and the *C. elegans* Reverse Genetics
864 Core Facility at the University of British Columbia, which is funded by the Canadian Institute for Health Research,
865 Genome Canada, Genome B.C., the Michael Smith Foundation, and the National Institutes of Health). Finally, we
866 thank the *Caenorhabditis* Genetics Center (CGC), which is funded by the NIH Office of Research Infrastructure
867 Programs (P40 OD010440), for providing strains.

868 References

869 Abramson, J., Adler, J., Dunger, J., Evans, R., Green, T., Pritzel, A., et al. (2024). Accurate structure prediction of biomolecular interactions
870 with AlphaFold 3. *Nature* 630(8016)**,** 493-500. doi: 10.1038/s41586-024-07487-w.

871 Aoki, I., Golinelli, L., Dunkel, E., Bhat, S., Bassam, E., Beets, I., et al. (2023). Hierarchical regulation of functionally antagonistic
872 neuropeptides expressed in a single neuron pair. *bioRxiv***,** 2023.2011.2023.568473. doi: 10.1101/2023.11.23.568473.

873 Bednarek, E.M., Schaheen, L., Gaubatz, J., Jorgensen, E.M., and Fares, H. (2007). The plasma membrane calcium ATPase MCA-3 is
874 required for clathrin-mediated endocytosis in scavenger cells of Caenorhabditis elegans. *Traffic* 8(5)**,** 543-553. doi: 10.1111/j.1600-
875 0854.2007.00547.x.

876 Berrocal, M., Corbacho, I., Sepulveda, M.R., Gutierrez-Merino, C., and Mata, A.M. (2017). Phospholipids and calmodulin modulate the
877 inhibition of PMCA activity by tau. *Biochim Biophys Acta Mol Cell Res* 1864(6)**,** 1028-1035. doi: 10.1016/j.bbamcr.2016.10.023.

878 Bhatla, N. (2012). "Exon-Intron Graphic Maker. Available at http://wormweb.org/exonintron.".).

879 Blazie, S.M., and Jin, Y. (2018). Pharming for Genes in Neurotransmission: Combining Chemical and Genetic Approaches in
880 Caenorhabditis elegans. *ACS Chem Neurosci* 9(8)**,** 1963-1974. doi: 10.1021/acschemneuro.7b00509.

881 Blumrich, E.M., Nicholson-Fish, J.C., Pronot, M., Davenport, E.C., Kurian, D., Cole, A., et al. (2023). Phosphatidylinositol 4-kinase IIalpha
882 is a glycogen synthase kinase 3-regulated interaction hub for activity-dependent bulk endocytosis. *Cell Rep* 42(6)**,** 112633. doi:
883 10.1016/j.celrep.2023.112633.

884 Boczek, T., Radzik, T., Ferenc, B., and Zylinska, L. (2019). The Puzzling Role of Neuron-Specific PMCA Isoforms in the Aging Process.
885 *Int J Mol Sci* 20(24). doi: 10.3390/ijms20246338.

886 Brenner, S. (1974). The genetics of Caenorhabditis elegans. *Genetics* 77(1)**,** 71-94. doi: 10.1093/genetics/77.1.71.

887 Brini, M., and Carafoli, E. (2011). The plasma membrane Ca(2)+ ATPase and the plasma membrane sodium calcium exchanger cooperate
888 in the regulation of cell calcium. *Cold Spring Harb Perspect Biol* 3(2). doi: 10.1101/cshperspect.a004168.

889 Brose, N., and Neher, E. (2009). Flowers for synaptic endocytosis. *Cell* 138(5)**,** 836-837. doi: 10.1016/j.cell.2009.08.023.

890 Calahorro, F., and Izquierdo, P.G. (2018). The presynaptic machinery at the synapse of C. elegans. *Invert Neurosci* 18(2)**,** 4. doi:
891 10.1007/s10158-018-0207-5.

892 Camara, D.F., Machado, M.L., Arantes, L.P., Silva, T.C., Silveira, T.L., Leal, J.G., et al. (2019). MPMT-OX up-regulates GABAergic
893 transmission and protects against seizure-like behavior in Caenorhabditis elegans. *Neurotoxicology* 74**,** 272-281. doi:
894 10.1016/j.neuro.2019.08.001.

895 Chamberland, S., Zamora Moratalla, A., and Topolnik, L. (2019). Calcium extrusion mechanisms in dendrites of mouse hippocampal CA1
896 inhibitory interneurons. *Cell Calcium* 77**,** 49-57. doi: 10.1016/j.ceca.2018.12.002.

897 Chang, H.F., Mannebach, S., Beck, A., Ravichandran, K., Krause, E., Frohnweiler, K., et al. (2018). Cytotoxic granule endocytosis depends
898 on the Flower protein. *J Cell Biol* 217(2)**,** 667-683. doi: 10.1083/jcb.201706053.

899 Chen, Z., Mondal, A., Abderemane-Ali, F., Jang, S., Niranjan, S., Montano, J.L., et al. (2023). EMC chaperone-Ca(V) structure reveals an
900 ion channel assembly intermediate. *Nature* 619(7969)**,** 410-419. doi: 10.1038/s41586-023-06175-5.

901 Clayton, E.L., Evans, G.J., and Cousin, M.A. (2008). Bulk synaptic vesicle endocytosis is rapidly triggered during strong stimulation. *J*
902 *Neurosci* 28(26)**,** 6627-6632. doi: 10.1523/JNEUROSCI.1445-08.2008.

903 Coelho, D.S., and Moreno, E. (2020). Neuronal Selection Based on Relative Fitness Comparison Detects and Eliminates Amyloid-beta-
904 Induced Hyperactive Neurons in Drosophila. *iScience* 23(9)**,** 101468. doi: 10.1016/j.isci.2020.101468.

905 Cong, D., Ren, J., Zhou, Y., Wang, S., Liang, J., Ding, M., et al. (2021). Motor domain-mediated autoinhibition dictates axonal transport
906 by the kinesin UNC-104/KIF1A. *PLoS Genet* 17(11)**,** e1009940. doi: 10.1371/journal.pgen.1009940.

907 Consortium, C.e.D.M. (2012). large-scale screening for targeted knockouts in the Caenorhabditis elegans genome. *G3 (Bethesda)* 2(11)**,**
908 1415-1425. doi: 10.1534/g3.112.003830.

909 Costa-Rodrigues, C., Couceiro, J., and Moreno, E. (2021). Cell competition from development to neurodegeneration. *Dis Model Mech*
910 14(7). doi: 10.1242/dmm.048926.

911 Cousin, M.A., and Robinson, P.J. (2001). The dephosphins: dephosphorylation by calcineurin triggers synaptic vesicle endocytosis. *Trends*
912 *Neurosci* 24(11)**,** 659-665. doi: 10.1016/s0166-2236(00)01930-5.

913 Cuentas-Condori, A., Chen, S., Krout, M., Gallik, K.L., Tipps, J., Gailey, C., et al. (2023). The epithelial Na(+) channel UNC-8 promotes
914 an endocytic mechanism that recycles presynaptic components to new boutons in remodeling neurons. *Cell Rep* 42(11)**,** 113327. doi:
915 10.1016/j.celrep.2023.113327.

916 Dai, Y., Taru, H., Deken, S.L., Grill, B., Ackley, B., Nonet, M.L., et al. (2006). SYD-2 Liprin-alpha organizes presynaptic active zone
917 formation through ELKS. *Nat Neurosci* 9(12)**,** 1479-1487. doi: 10.1038/nn1808.

918 Duncan, A.L., Song, W., and Sansom, M.S.P. (2020). Lipid-Dependent Regulation of Ion Channels and G Protein-Coupled Receptors:
919 Insights from Structures and Simulations. *Annu Rev Pharmacol Toxicol* 60**,** 31-50. doi: 10.1146/annurev-pharmtox-010919-023411.

920 Eberhardt, J., Santos-Martins, D., Tillack, A.F., and Forli, S. (2021). AutoDock Vina 1.2.0: New Docking Methods, Expanded Force Field,
921 and Python Bindings. *J Chem Inf Model* 61(8)**,** 3891-3898. doi: 10.1021/acs.jcim.1c00203.

922 Edelstein, A.D., Tsuchida, M.A., Amodaj, N., Pinkard, H., Vale, R.D., and Stuurman, N. (2014). Advanced methods of microscope control
923 using muManager software. *J Biol Methods* 1(2). doi: 10.14440/jbm.2014.36.

924 Evans, R., O'Neill, M., Pritzel, A., Antropova, N., Senior, A., Green, T., et al. (2022). Protein complex prediction with AlphaFold-Multimer.
925 *bioRxiv***,** 2021.2010.2004.463034. doi: 10.1101/2021.10.04.463034.

926 Fares, H., and Grant, B. (2002). Deciphering endocytosis in Caenorhabditis elegans. *Traffic* 3(1)**,** 11-19. doi: 10.1034/j.1600-
927 0854.2002.30103.x.

Fares, H., and Greenwald, I. (2001). Genetic analysis of endocytosis in Caenorhabditis elegans: coelomocyte uptake defective mutants. *Genetics* 159(1)**,** 133-145. doi: 10.1093/genetics/159.1.133.

Filoteo, A.G., Enyedi, A., and Penniston, J.T. (1992). The lipid-binding peptide from the plasma membrane Ca2+ pump binds calmodulin, and the primary calmodulin-binding domain interacts with lipid. *J Biol Chem* 267(17)**,** 11800-11805.

Fire, A. (1986). Integrative transformation of Caenorhabditis elegans. *EMBO J* 5(10)**,** 2673-2680. doi: 10.1002/j.1460-2075.1986.tb04550.x.

Fleming, J.T., Squire, M.D., Barnes, T.M., Tornoe, C., Matsuda, K., Ahnn, J., et al. (1997). Caenorhabditis elegans levamisole resistance genes lev-1, unc-29, and unc-38 encode functional nicotinic acetylcholine receptor subunits. *J Neurosci* 17(15)**,** 5843-5857. doi: 10.1523/JNEUROSCI.17-15-05843.1997.

Gally, C., and Bessereau, J.L. (2003). GABA is dispensable for the formation of junctional GABA receptor clusters in Caenorhabditis elegans. *J Neurosci* 23(7)**,** 2591-2599. doi: 10.1523/JNEUROSCI.23-07-02591.2003.

Gan, Q., and Watanabe, S. (2018). Synaptic Vesicle Endocytosis in Different Model Systems. *Front Cell Neurosci* 12**,** 171. doi: 10.3389/fncel.2018.00171.

Gottschalk, A., Almedom, R.B., Schedletzky, T., Anderson, S.D., Yates, J.R., 3rd, and Schafer, W.R. (2005). Identification and characterization of novel nicotinic receptor-associated proteins in Caenorhabditis elegans. *EMBO J* 24(14)**,** 2566-2578. doi: 10.1038/sj.emboj.7600741.

Gross, O.P., and von Gersdorff, H. (2016). Recycling at synapses. *Elife* 5. doi: 10.7554/eLife.17692.

Hall, D.H., and Hedgecock, E.M. (1991). Kinesin-related gene unc-104 is required for axonal transport of synaptic vesicles in C. elegans. *Cell* 65(5)**,** 837-847. doi: 10.1016/0092-8674(91)90391-b.

Hallgren, J., Tsirigos, K.D., Pedersen, M.D., Almagro Armenteros, J.J., Marcatili, P., Nielsen, H., et al. (2022). DeepTMHMM predicts alpha and beta transmembrane proteins using deep neural networks. *bioRxiv***,** 2022.2004.2008.487609. doi: 10.1101/2022.04.08.487609.

Hansen, S.B., Tao, X., and MacKinnon, R. (2011). Structural basis of PIP2 activation of the classical inward rectifier K+ channel Kir2.2. *Nature* 477(7365)**,** 495-498. doi: 10.1038/nature10370.

Haucke, V., Neher, E., and Sigrist, S.J. (2011). Protein scaffolds in the coupling of synaptic exocytosis and endocytosis. *Nat Rev Neurosci* 12(3)**,** 127-138. doi: 10.1038/nrn2948.

Hoenderop, J.G., Voets, T., Hoefs, S., Weidema, F., Prenen, J., Nilius, B., et al. (2003). Homo- and heterotetrameric architecture of the epithelial Ca2+ channels TRPV5 and TRPV6. *EMBO J* 22(4)**,** 776-785. doi: 10.1093/emboj/cdg080.

Janosi, B., Liewald, J.F., Seidenthal, M., Yu, S.C., Umbach, S., Redzovic, J., et al. (2024). RIM and RIM-Binding Protein Localize Synaptic CaV2 Channels to Differentially Regulate Transmission in Neuronal Circuits. *J Neurosci* 44(31). doi: 10.1523/JNEUROSCI.0535-22.2024.

Katan, M., and Cockcroft, S. (2020). Phosphatidylinositol(4,5)bisphosphate: diverse functions at the plasma membrane. *Essays Biochem* 64(3)**,** 513-531. doi: 10.1042/EBC20200041.

Kittelmann, M., Hegermann, J., Goncharov, A., Taru, H., Ellisman, M.H., Richmond, J.E., et al. (2013a). Liprin-alpha/SYD-2 determines the size of dense projections in presynaptic active zones in C. elegans. *J Cell Biol* 203(5)**,** 849-863. doi: 10.1083/jcb.201302022.

Kittelmann, M., Liewald, J.F., Hegermann, J., Schultheis, C., Brauner, M., Steuer Costa, W., et al. (2013b). In vivo synaptic recovery following optogenetic hyperstimulation. *Proc Natl Acad Sci U S A* 110(32)**,** E3007-3016. doi: 10.1073/pnas.1305679110.

Klopfenstein, D.R., and Vale, R.D. (2004). The lipid binding pleckstrin homology domain in UNC-104 kinesin is necessary for synaptic vesicle transport in Caenorhabditis elegans. *Mol Biol Cell* 15(8)**,** 3729-3739. doi: 10.1091/mbc.e04-04-0326.

Kraev, A., Kraev, N., and Carafoli, E. (1999). Identification and functional expression of the plasma membrane calcium ATPase gene family from Caenorhabditis elegans. *J Biol Chem* 274(7)**,** 4254-4258. doi: 10.1074/jbc.274.7.4254.

Krebs, J. (2022). Structure, Function and Regulation of the Plasma Membrane Calcium Pump in Health and Disease. *Int J Mol Sci* 23(3). doi: 10.3390/ijms23031027.

Krick, N., Ryglewski, S., Pichler, A., Bikbaev, A., Gotz, T., Kobler, O., et al. (2021). Separation of presynaptic Ca(v)2 and Ca(v)1 channel function in synaptic vesicle exo- and endocytosis by the membrane anchored Ca(2+) pump PMCA. *Proc Natl Acad Sci U S A* 118(28). doi: 10.1073/pnas.2106621118.

Kumashiro, S., Lu, Y.F., Tomizawa, K., Matsushita, M., Wei, F.Y., and Matsui, H. (2005). Regulation of synaptic vesicle recycling by calcineurin in different vesicle pools. *Neurosci Res* 51(4)**,** 435-443. doi: 10.1016/j.neures.2004.12.018.

Larkin, M.A., Blackshields, G., Brown, N.P., Chenna, R., McGettigan, P.A., McWilliam, H., et al. (2007). Clustal W and Clustal X version 2.0. *Bioinformatics* 23(21)**,** 2947-2948. doi: 10.1093/bioinformatics/btm404.

977 Leitz, J., and Kavalali, E.T. (2016). Ca2+ Dependence of Synaptic Vesicle Endocytosis. *Neuroscientist* 22(5)**,** 464-476. doi:
978 10.1177/1073858415588265.

979 Li, T.N., Chen, Y.J., Lu, T.Y., Wang, Y.T., Lin, H.C., and Yao, C.K. (2020). A positive feedback loop between Flower and PI(4,5)P(2) at
980 periactive zones controls bulk endocytosis in Drosophila. *Elife* 9. doi: 10.7554/eLife.60125.

981 Liewald, J.F., Brauner, M., Stephens, G.J., Bouhours, M., Schultheis, C., Zhen, M., et al. (2008). Optogenetic analysis of synaptic function.
982 *Nat Methods* 5(10)**,** 895-902. doi: 10.1038/nmeth.1252.

983 Liu, Q., Chen, B., Yankova, M., Morest, D.K., Maryon, E., Hand, A.R., et al. (2005). Presynaptic ryanodine receptors are required for
984 normal quantal size at the Caenorhabditis elegans neuromuscular junction. *J Neurosci* 25(29)**,** 6745-6754. doi:
985 10.1523/JNEUROSCI.1730-05.2005.

986 Lopreiato, R., Giacomello, M., and Carafoli, E. (2014). The plasma membrane calcium pump: new ways to look at an old enzyme. *J Biol*
987 *Chem* 289(15)**,** 10261-10268. doi: 10.1074/jbc.O114.555565.

988 Lou, X. (2018). Sensing Exocytosis and Triggering Endocytosis at Synapses: Synaptic Vesicle Exocytosis-Endocytosis Coupling. *Front*
989 *Cell Neurosci* 12**,** 66. doi: 10.3389/fncel.2018.00066.

990 Lu, Y., Ahamed, T., Mulcahy, B., Meng, J., Witvliet, D., Guan, S.A., et al. (2022). Extrasynaptic signaling enables an asymmetric juvenile
991 motor circuit to produce symmetric undulation. *Curr Biol* 32(21)**,** 4631-4644 e4635. doi: 10.1016/j.cub.2022.09.002.

992 Madan, E., Pelham, C.J., Nagane, M., Parker, T.M., Canas-Marques, R., Fazio, K., et al. (2019). Flower isoforms promote competitive
993 growth in cancer. *Nature* 572(7768)**,** 260-264. doi: 10.1038/s41586-019-1429-3.

994 Mahoney, T.R., Luo, S., and Nonet, M.L. (2006). Analysis of synaptic transmission in Caenorhabditis elegans using an aldicarb-sensitivity
995 assay. *Nat Protoc* 1(4)**,** 1772-1777. doi: 10.1038/nprot.2006.281.

996 Mantilla, G., Perez-Gordones, M.C., Cisneros-Montufar, S., Benaim, G., Navarro, J.C., Mendoza, M., et al. (2023). Structural Analysis and
997 Diversity of Calmodulin-Binding Domains in Membrane and Intracellular Ca(2+)-ATPases. *J Membr Biol* 256(2)**,** 159-174. doi:
998 10.1007/s00232-022-00275-5.

999 Miller-Fleming, T.W., Petersen, S.C., Manning, L., Matthewman, C., Gornet, M., Beers, A., et al. (2016). The DEG/ENaC cation channel
1000 protein UNC-8 drives activity-dependent synapse removal in remodeling GABAergic neurons. *Elife* 5. doi: 10.7554/eLife.14599.

1001 Nagel, G., Brauner, M., Liewald, J.F., Adeishvili, N., Bamberg, E., and Gottschalk, A. (2005). Light activation of channelrhodopsin-2 in
1002 excitable cells of Caenorhabditis elegans triggers rapid behavioral responses. *Curr Biol* 15(24)**,** 2279-2284. doi:
1003 10.1016/j.cub.2005.11.032.

1004 Nakai, J., Ohkura, M., and Imoto, K. (2001). A high signal-to-noise Ca(2+) probe composed of a single green fluorescent protein. *Nat*
1005 *Biotechnol* 19(2)**,** 137-141. doi: 10.1038/84397.

1006 Nonet, M.L. (1999). Visualization of synaptic specializations in live C. elegans with synaptic vesicle protein-GFP fusions. *J Neurosci*
1007 *Methods* 89(1)**,** 33-40. doi: 10.1016/s0165-0270(99)00031-x.

1008 Nussbaum-Krammer, C.I., Neto, M.F., Brielmann, R.M., Pedersen, J.S., and Morimoto, R.I. (2015). Investigating the spreading and toxicity
1009 of prion-like proteins using the metazoan model organism C. elegans. *J Vis Exp* (95)**,** 52321. doi: 10.3791/52321.

1010 Oda, K., Vierock, J., Oishi, S., Rodriguez-Rozada, S., Taniguchi, R., Yamashita, K., et al. (2018). Crystal structure of the red light-activated
1011 channelrhodopsin Chrimson. *Nat Commun* 9(1)**,** 3949. doi: 10.1038/s41467-018-06421-9.

1012 Okamoto, Y., Lipstein, N., Hua, Y., Lin, K.H., Brose, N., Sakaba, T., et al. (2016). Distinct modes of endocytotic presynaptic membrane
1013 and protein uptake at the calyx of Held terminal of rats and mice. *Elife* 5. doi: 10.7554/eLife.14643.

1014 Ono, Y., Mori, Y., Egashira, Y., Sumiyama, K., and Takamori, S. (2019). Expression of plasma membrane calcium ATPases confers
1015 Ca(2+)/H(+) exchange in rodent synaptic vesicles. *Sci Rep* 9(1)**,** 4289. doi: 10.1038/s41598-019-40557-y.

1016 Penniston, J.T., Padanyi, R., Paszty, K., Varga, K., Hegedus, L., and Enyedi, A. (2014). Apart from its known function, the plasma
1017 membrane Ca(2)(+)ATPase can regulate Ca(2)(+) signaling by controlling phosphatidylinositol 4,5-bisphosphate levels. *J Cell Sci*
1018 127(Pt 1)**,** 72-84. doi: 10.1242/jcs.132548.

1019 Petrova, E., Lopez-Gay, J.M., Rhiner, C., and Moreno, E. (2012). Flower-deficient mice have reduced susceptibility to skin papilloma
1020 formation. *Dis Model Mech* 5(4)**,** 553-561. doi: 10.1242/dmm.008623.

1021 Posor, Y., Eichhorn-Grunig, M., and Haucke, V. (2015). Phosphoinositides in endocytosis. *Biochim Biophys Acta* 1851(6)**,** 794-804. doi:
1022 10.1016/j.bbalip.2014.09.014.

1023 Rhiner, C., Lopez-Gay, J.M., Soldini, D., Casas-Tinto, S., Martin, F.A., Lombardia, L., et al. (2010). Flower forms an extracellular code
1024 that reveals the fitness of a cell to its neighbors in Drosophila. *Dev Cell* 18(6)**,** 985-998. doi: 10.1016/j.devcel.2010.05.010.

1025 Ribalet, B., John, S.A., Xie, L.H., and Weiss, J.N. (2005). Regulation of the ATP-sensitive K channel Kir6.2 by ATP and PIP(2). *J Mol*
1026 *Cell Cardiol* 39(1)**,** 71-77. doi: 10.1016/j.yjmcc.2004.11.018.

1027 Richmond, J.E., and Jorgensen, E.M. (1999). One GABA and two acetylcholine receptors function at the C. elegans neuromuscular junction.
1028 *Nat Neurosci* 2(9)**,** 791-797. doi: 10.1038/12160.

1029 Rohacs, T. (2024). Phosphoinositide Regulation of TRP Channels: A Functional Overview in the Structural Era. *Annu Rev Physiol* 86**,** 329-
1030 355. doi: 10.1146/annurev-physiol-042022-013956.

1031 Rosignoli, S., and Paiardini, A. (2022). DockingPie: a consensus docking plugin for PyMOL. *Bioinformatics* 38(17)**,** 4233-4234. doi:
1032 10.1093/bioinformatics/btac452.

1033 Rudd, J.C., Maity, S., Grunkemeyer, J.A., Snyder, J.C., Lovas, S., and Hansen, L.A. (2023). Membrane structure and internalization
1034 dynamics of human Flower isoforms hFWE3 and hFWE4 indicate a conserved endocytic role for hFWE4. *J Biol Chem* 299(8)**,** 104945.
1035 doi: 10.1016/j.jbc.2023.104945.

1036 Salcini, A.E., Hilliard, M.A., Croce, A., Arbucci, S., Luzzi, P., Tacchetti, C., et al. (2001). The Eps15 C. elegans homologue EHS-1 is
1037 implicated in synaptic vesicle recycling. *Nat Cell Biol* 3(8)**,** 755-760. doi: 10.1038/35087075.

1038 Sankaranarayanan, S., De Angelis, D., Rothman, J.E., and Ryan, T.A. (2000). The use of pHluorins for optical measurements of presynaptic
1039 activity. *Biophys J* 79(4)**,** 2199-2208. doi: 10.1016/S0006-3495(00)76468-X.

1040 Sattelle, D.B., Culetto, E., Grauso, M., Raymond, V., Franks, C.J., and Towers, P. (2002). Functional genomics of ionotropic acetylcholine
1041 receptors in Caenorhabditis elegans and Drosophila melanogaster. *Novartis Found Symp* 245**,** 240-257; discussion 257-260, 261-244.

1042 Schultheis, C., Brauner, M., Liewald, J.F., and Gottschalk, A. (2011). Optogenetic analysis of GABAB receptor signaling in Caenorhabditis
1043 elegans motor neurons. *J Neurophysiol* 106(2)**,** 817-827. doi: 10.1152/jn.00578.2010.

1044 Schuske, K.R., Richmond, J.E., Matthies, D.S., Davis, W.S., Runz, S., Rube, D.A., et al. (2003). Endophilin is required for synaptic vesicle
1045 endocytosis by localizing synaptojanin. *Neuron* 40(4)**,** 749-762. doi: 10.1016/s0896-6273(03)00667-6.

1046 Seidenthal, M., Janosi, B., Rosenkranz, N., Schuh, N., Elvers, N., Willoughby, M., et al. (2023). pOpsicle: An all-optical reporter system
1047 for synaptic vesicle recycling combining pH-sensitive fluorescent proteins with optogenetic manipulation of neuronal activity. *Front*
1048 *Cell Neurosci* 17**,** 1120651. doi: 10.3389/fncel.2023.1120651.

1049 Seidenthal, M., Vettkotter, D., and Gottschalk, A. (2022). WormRuler: A software to track body length used to characterize a super red-
1050 shifted channelrhodopsin in Caenorhabditis elegans. *MicroPubl Biol* 2022. doi: 10.17912/micropub.biology.000607.

1051 Swierczek, N.A., Giles, A.C., Rankin, C.H., and Kerr, R.A. (2011). High-throughput behavioral analysis in C. elegans. *Nat Methods* 8(7)**,**
1052 592-598. doi: 10.1038/nmeth.1625.

1053 Taylor, S.R., Santpere, G., Weinreb, A., Barrett, A., Reilly, M.B., Xu, C., et al. (2021). Molecular topography of an entire nervous system.
1054 *Cell* 184(16)**,** 4329-4347 e4323. doi: 10.1016/j.cell.2021.06.023.

1055 Vashlishan, A.B., Madison, J.M., Dybbs, M., Bai, J., Sieburth, D., Ch'ng, Q., et al. (2008). An RNAi screen identifies genes that regulate
1056 GABA synapses. *Neuron* 58(3)**,** 346-361. doi: 10.1016/j.neuron.2008.02.019.

1057 Vettkotter, D., Schneider, M., Goulden, B.D., Dill, H., Liewald, J., Zeiler, S., et al. (2022). Rapid and reversible optogenetic silencing of
1058 synaptic transmission by clustering of synaptic vesicles. *Nat Commun* 13(1)**,** 7827. doi: 10.1038/s41467-022-35324-z.

1059 Ward, S., Thomson, N., White, J.G., and Brenner, S. (1975). Electron microscopical reconstruction of the anterior sensory anatomy of the
1060 nematode Caenorhabditis elegans. *J Comp Neurol* 160(3)**,** 313-337. doi: 10.1002/cne.901600305.

1061 Watanabe, S., Davis, M.W., Kusick, G.F., Iwasa, J., and Jorgensen, E.M. (2020). SynapsEM: Computer-Assisted Synapse Morphometry.
1062 *Front Synaptic Neurosci* 12**,** 584549. doi: 10.3389/fnsyn.2020.584549.

1063 Watanabe, S., Liu, Q., Davis, M.W., Hollopeter, G., Thomas, N., Jorgensen, N.B., et al. (2013). Ultrafast endocytosis at Caenorhabditis
1064 elegans neuromuscular junctions. *Elife* 2**,** e00723. doi: 10.7554/eLife.00723.

1065 Watanabe, S., Trimbuch, T., Camacho-Perez, M., Rost, B.R., Brokowski, B., Sohl-Kielczynski, B., et al. (2014). Clathrin regenerates
1066 synaptic vesicles from endosomes. *Nature* 515(7526)**,** 228-233. doi: 10.1038/nature13846.

1067 Weimer, R.M. (2006). Preservation of C. elegans tissue via high-pressure freezing and freeze-substitution for ultrastructural analysis and
1068 immunocytochemistry. *Methods Mol Biol* 351**,** 203-221. doi: 10.1385/1-59745-151-7:203.

1069 Weissenberger, S., Schultheis, C., Liewald, J.F., Erbguth, K., Nagel, G., and Gottschalk, A. (2011). PACalpha--an optogenetic tool for in
1070 vivo manipulation of cellular cAMP levels, neurotransmitter release, and behavior in Caenorhabditis elegans. *J Neurochem* 116(4)**,** 616-
1071 625. doi: 10.1111/j.1471-4159.2010.07148.x.

1072 Wu, L.G., and Betz, W.J. (1998). Kinetics of synaptic depression and vesicle recycling after tetanic stimulation of frog motor nerve
1073 terminals. *Biophys J* 74(6)**,** 3003-3009. doi: 10.1016/S0006-3495(98)78007-5.

1074 Wu, X.S., McNeil, B.D., Xu, J., Fan, J., Xue, L., Melicoff, E., et al. (2009). Ca(2+) and calmodulin initiate all forms of endocytosis during
1075 depolarization at a nerve terminal. *Nat Neurosci* 12(8)**,** 1003-1010. doi: 10.1038/nn.2355.

1076 Wu, Y., O'Toole, E.T., Girard, M., Ritter, B., Messa, M., Liu, X., et al. (2014). A dynamin 1-, dynamin 3- and clathrin-independent pathway
1077 of synaptic vesicle recycling mediated by bulk endocytosis. *Elife* 3**,** e01621. doi: 10.7554/eLife.01621.

1078 Xue, L., Zhang, Z., McNeil, B.D., Luo, F., Wu, X.S., Sheng, J., et al. (2012). Voltage-dependent calcium channels at the plasma membrane,
1079 but not vesicular channels, couple exocytosis to endocytosis. *Cell Rep* 1(6)**,** 632-638. doi: 10.1016/j.celrep.2012.04.011.

1080 Yamashita, T. (2012). Ca2+-dependent regulation of synaptic vesicle endocytosis. *Neurosci Res* 73(1)**,** 1-7. doi:
1081 10.1016/j.neures.2012.02.012.

1082 Yao, C.K., Lin, Y.Q., Ly, C.V., Ohyama, T., Haueter, C.M., Moiseenkova-Bell, V.Y., et al. (2009). A synaptic vesicle-associated Ca2+
1083 channel promotes endocytosis and couples exocytosis to endocytosis. *Cell* 138(5)**,** 947-960. doi: 10.1016/j.cell.2009.06.033.

1084 Yao, C.K., Liu, Y.T., Lee, I.C., Wang, Y.T., and Wu, P.Y. (2017). A Ca2+ channel differentially regulates Clathrin-mediated and activity-
1085 dependent bulk endocytosis. *PLoS Biol* 15(4)**,** e2000931. doi: 10.1371/journal.pbio.2000931.

1086 Yu, S.C., Janosi, B., Liewald, J.F., Wabnig, S., and Gottschalk, A. (2018). Endophilin A and B Join Forces With Clathrin to Mediate
1087 Synaptic Vesicle Recycling in Caenorhabditis elegans. *Front Mol Neurosci* 11**,** 196. doi: 10.3389/fnmol.2018.00196.

1088 Zhang, M., Ma, Y., Ye, X., Zhang, N., Pan, L., and Wang, B. (2023). TRP (transient receptor potential) ion channel family: structures,
1089 biological functions and therapeutic interventions for diseases. *Signal Transduct Target Ther* 8(1)**,** 261. doi: 10.1038/s41392-023-
1090 01464-x.

1091

1092

1093 # SUPPLEMENTAL FIGURES

1094 **Supplementary Table 1: Plasmids used in this study.**

1095 **Supplementary Table 2: Strains used in this study.**

1096 **Supplementary Table 3: CeNGEN expression data of *flwr-1/F20D1.1* and *mca-3***

1097 Single-cell RNAseq data as described in Taylor et al. (2021). The threshold was set to "All Cells Unfiltered". Cell types were sorted
1098 alphabetically. Where CeNGEN did not produce any results, cells were left blank.

1099 **Supplementary Movie 1.**

1100 Time series of a particle containing GFP::FLWR-1 and mCherry::SNB-1 travelling along commissures. Scale bar, 2 µm.

1101

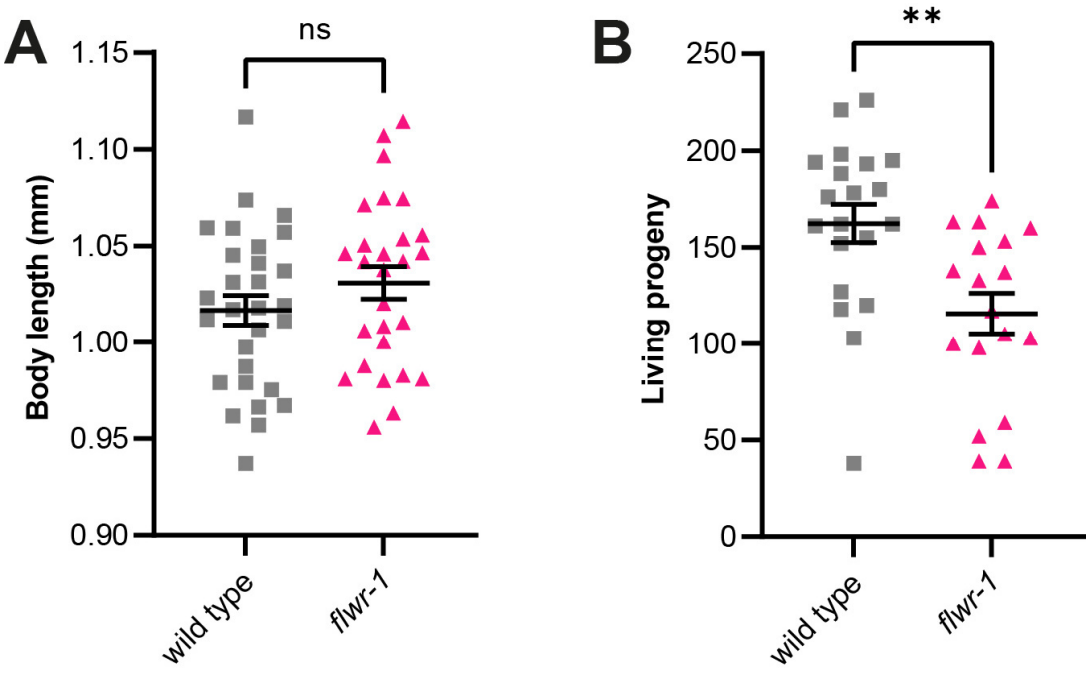

1102

1103 **Fig. S1. Loss of FLWR-1 does not change body length but reduces number of living progeny.**

1104 **(A)** Mean (± SEM) body length of wild type and *flwr-1(ok3128)* mutants in mm. Unpaired t-test. ns not significant. Number of animals
1105 accumulated from N = 4 biological replicates: wild type = 29, *flwr-1* = 27. **(B)** Mean (± SEM) number of living progeny per animal.
1106 Unpaired t-test. ** $p < 0.01$. Number of animals accumulated from N = 4 biological replicates: wild type = 20, *flwr-1* = 18.

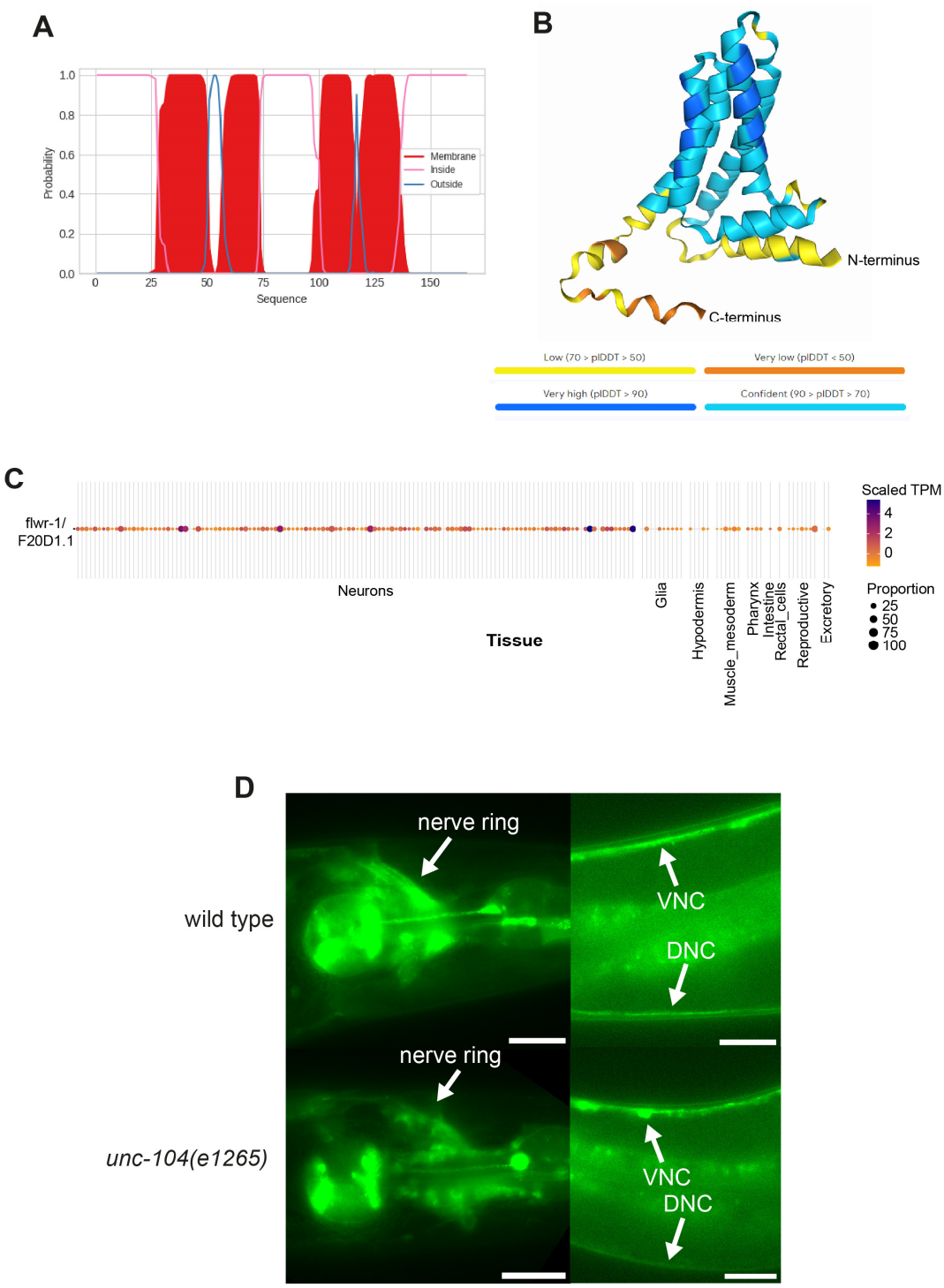

Fig. S2. FLWR-1 is predicted to be a tetraspan transmembrane protein and is transported by UNC-104 kinesin.

(A) Graphical representation of the results of DeepTMHMM prediction of membrane orientation of the FLWR-1 protein based on its amino acid sequence. The red shapes indicate the presence of four transmembrane domains. **(B)** Alphafold3 prediction of FLWR-1 protein structure. The coloring represents the calculated predicted local distance difference test (plDDT) as shown below the structure. Higher plDDT values indicate a higher confidence of correct prediction. **(C)** Heatmap plot depicting *flwr-1(F20D1.1)* single-cell RNAseq data generated by the CeNGEN database. Coloring indicates transcripts per million (TPM) per tissue normalized to the average expression as indicated in the legend. The size of the dots represents the percentage of cells of this cell type expressing the gene. **(D)** Example images depicting GFP::FLWR-1 fluorescence in nerve ring and nerve cords in wild type and *unc-104(e1265)* mutants. Scale bar, 20µm.

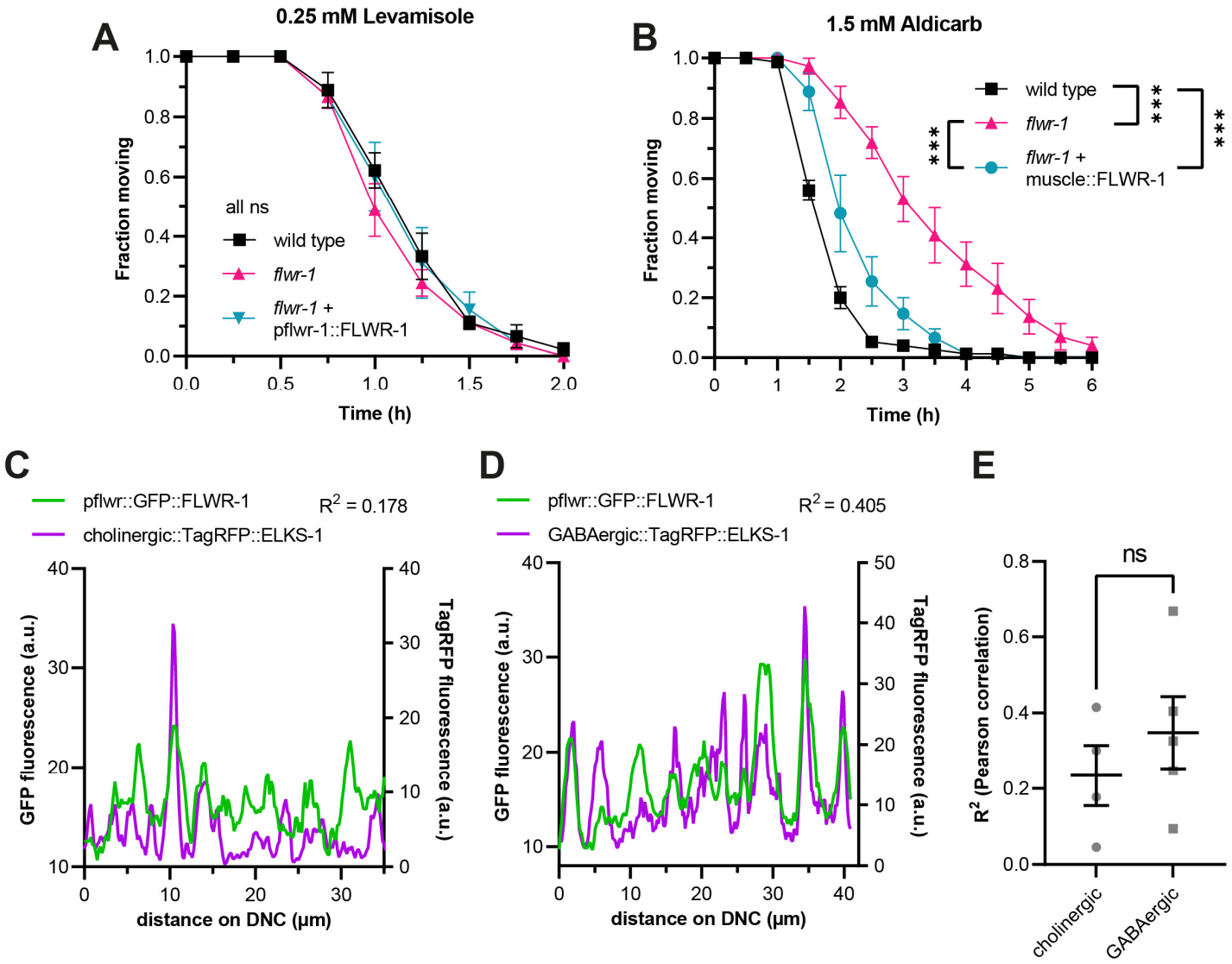

Fig. S3. FLWR-1 expression in body wall muscle cells partially rescues aldicarb resistance of *flwr-1* mutants; FLWR-1 localizes to cholinergic and GABAergic active zones.

(**A**) Mean (± SEM) fraction of moving animals after exposure to 0.25 mM levamisole. N = 3 biological replicates. **(B)** Mean (± SEM) fraction of moving animals after exposure to 1.5 mM aldicarb with expression of FLWR-1 in BWMs (*pmyo-3*) in *flwr-1(ok3128)* mutant background. N = 5 biological replicates. **(A + B)** Two-way ANOVAs with Tukey's correction. There were no significant differences in (A); *** $p < 0.001$. **(C)** Line scan analysis of colocalization of GFP::FLWR-1 and TagRFP::ELKS-1 along the DNC as represented in the uppermost micrographs in **Fig. 3A**. R^2 as determined by Pearson correlation. a.u. = arbitrary units of fluorescence intensity. **(D)** Line scan analysis of colocalization of GFP::FLWR-1 and TagRFP::ELKS-1 along the DNC as represented in the uppermost micrographs in **Fig. 3B**. R^2 as determined by Pearson correlation. a.u. = arbitrary units of fluorescence intensity. **(E)** Comparison of Pearson correlation coefficients of line scans along DNCs represented in **Fig. 3**. Mean (± SEM). Unpaired t-test.

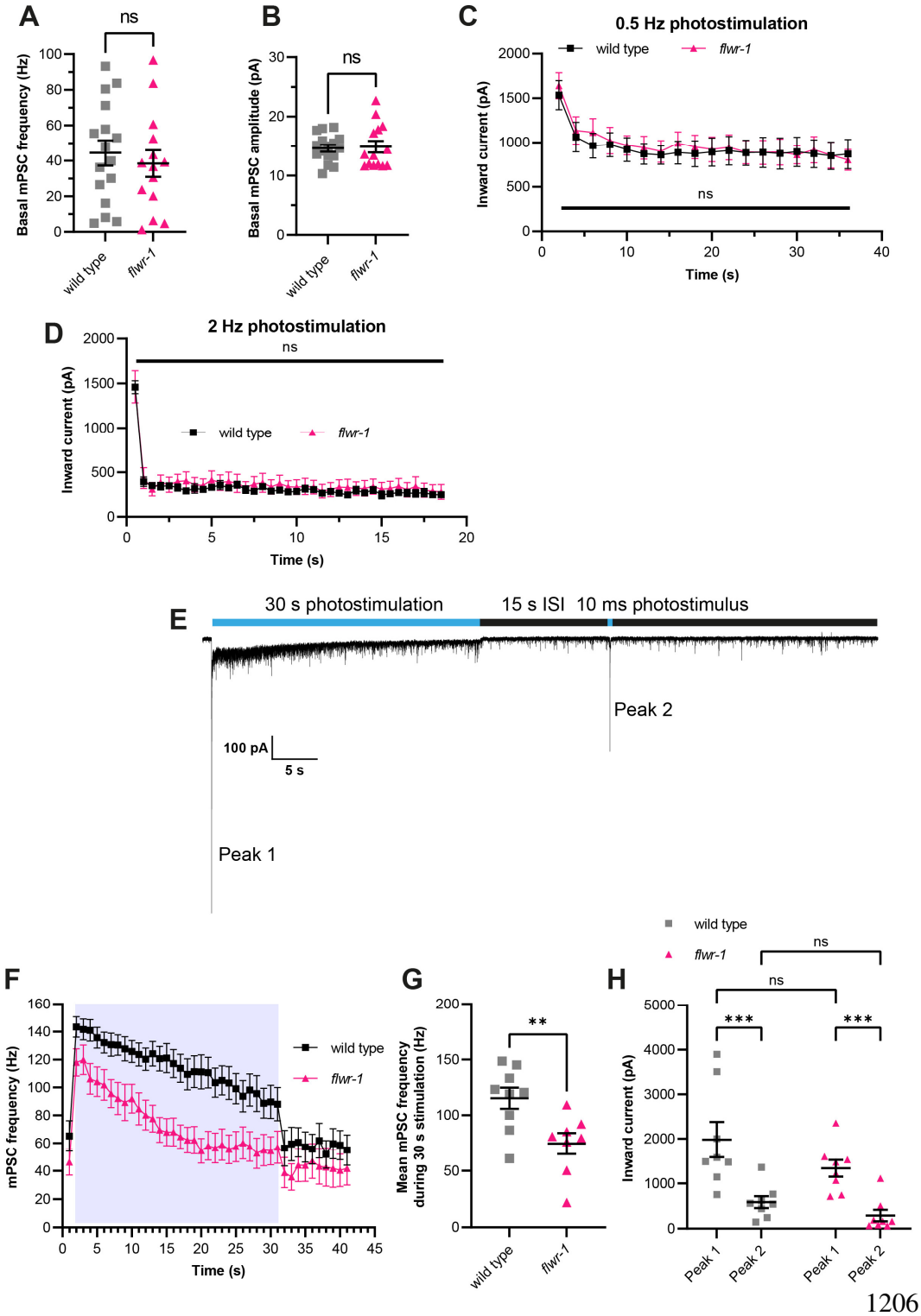

Fig. S4. *flwr-1* mutants show defecting cholinergic neurotransmission only during continuous stimulation.

(A, B) Mean (± SEM) mPSC frequency and amplitude, respectively, before stimulation. Unpaired t-test. ns not significant. Number of animals: wild type = 16, *flwr-1* = 14. **(C)** Mean (± SEM) inward currents of BWMs recordings induced by 10 ms light pulses (470 nm, 8 mW/mm^2) applied every 2 s (0.5 Hz). Two-way ANOVA with Šidák's correction for multiple comparisons. ns not significant. Number of animals: wild type = 9, *flwr-1* = 8. **(D)** As in (C), but 2Hz stimulation. ns not significant. Number of animals: wild type = 7, *flwr-1* = 7. **(E)** Representative voltage-clamp recording of currents detected in BWMs. This wild type animal expresses ChR2(H134R) in cholinergic motor neurons (*unc-17* promoter) and has been treated with ATR. A 30 s light stimulus (470 nm, 8 mW/mm^2) as well as a 10 ms pulse after a 15 s inter-stimulus interval (ISI) were applied as indicated by blue bars. **(F)** Mean (± SEM) mPSC frequency in BWMs of animals expressing ChR2(H134R) in cholinergic motor neurons (*unc-17* promoter). All animals have been treated with ATR. A 30 s light pulse (470 nm, 8 mW/mm^2) was applied as indicated by blue shade. **(G)** Mean (± SEM) mPSC frequency during 30 s stimulation. Unpaired t-test. * $p < 0.05$. **(H)** Analysis of the amplitude of the first peak during 30 s photostimulation and the second peak after 15 s ISI as indicated in (E). Two-way ANOVA with Tukey's correction for multiple comparisons. ns not significant, *** $p < 0.001$. (F - H) Number of animals: wild type = 9, *flwr-1* = 8.

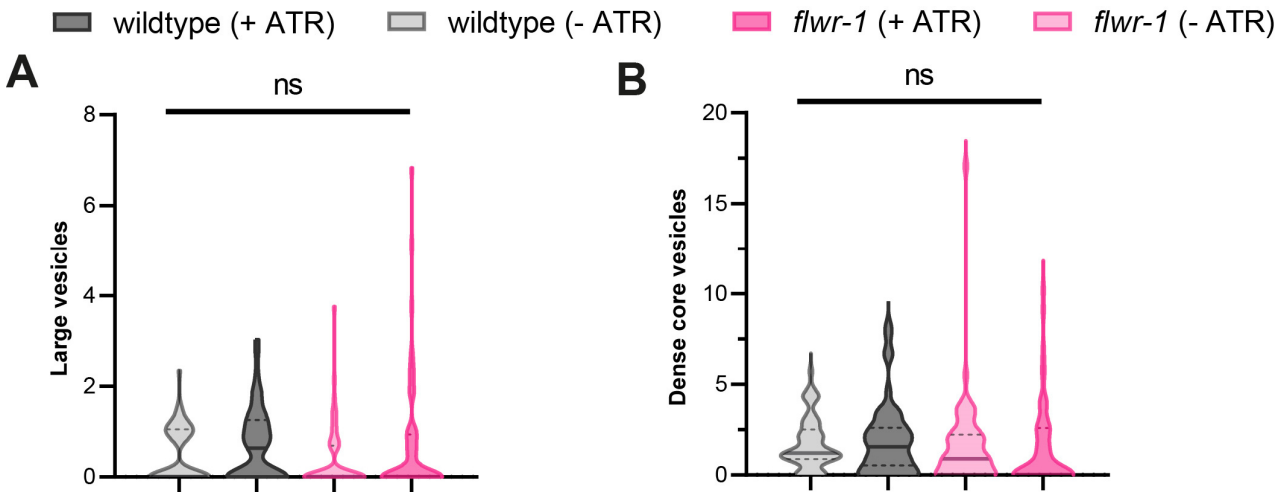

1210

1211 **Fig. S5 *flwr-1* mutants have a normal number of large vesicles and dense core vesicles before and after stimulation.**

1212 **(A)** Violin plot depicting the number of large vesicles counted per synaptic profile. **(B)** Violin plot depicting the number of dense core
1213 vesicles counted per synaptic profile. **(A + B)** Bold line represents the median and the dashed lines the IQR. Kruskal-Wallis test. Only
1214 significant statistical differences are depicted. ns not significant. Number of synaptic profiles imaged: wild type (-ATR) = 56, wild type (-
1215 ATR) = 51, *flwr-1* (-ATR) = 55, *flwr-1* (+ATR) = 59.

1216

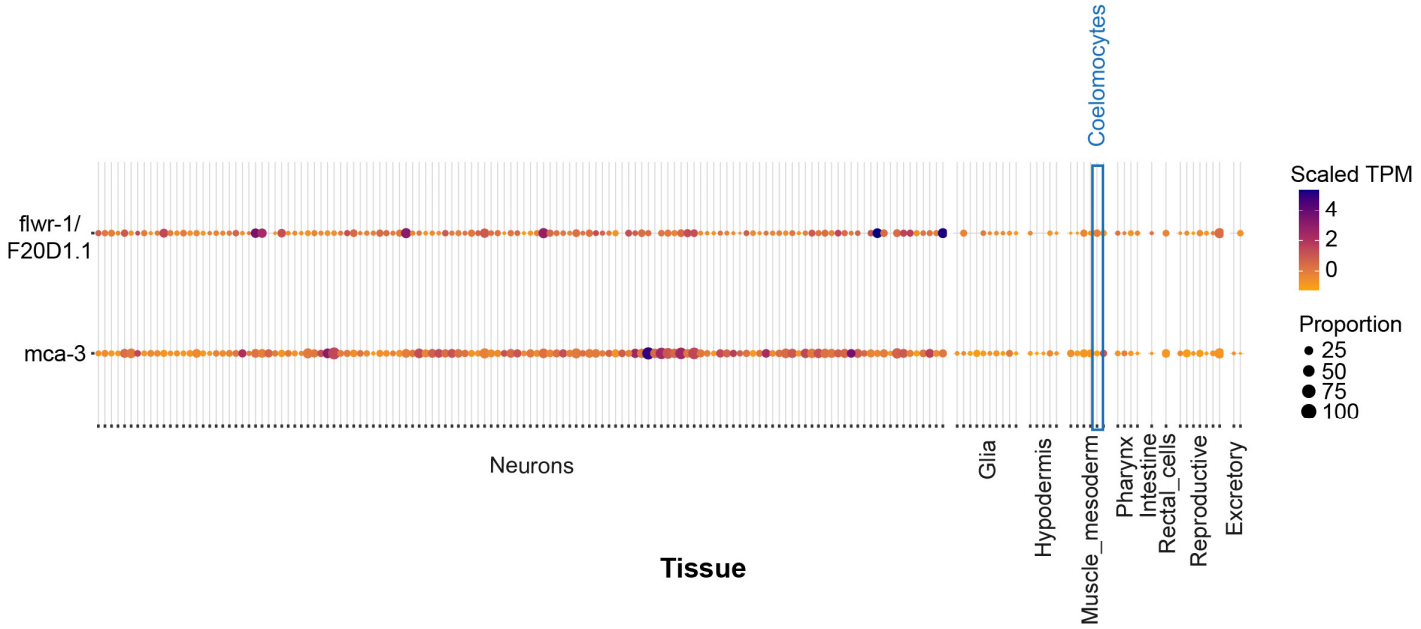

1217

1218 **Fig. S6. Comparison of *flwr-1* and *mca-3* expression by single-cell RNAseq data.**

1219 Heatmap plot depicting *flwr-1(F20D1.1)* and *mca-3* single-cell RNAseq data generated by the CeNGEN database
1220 (https://cengen.shinyapps.io/CengenApp/). Coloring indicates transcripts per million (TPM) per tissue normalized to the average expression
1221 as indicated in the legend. The size of the dots represents the percentage of cells of this cell type expressing the gene. Coelomocyte data is
1222 highlighted by the blue box.

1223

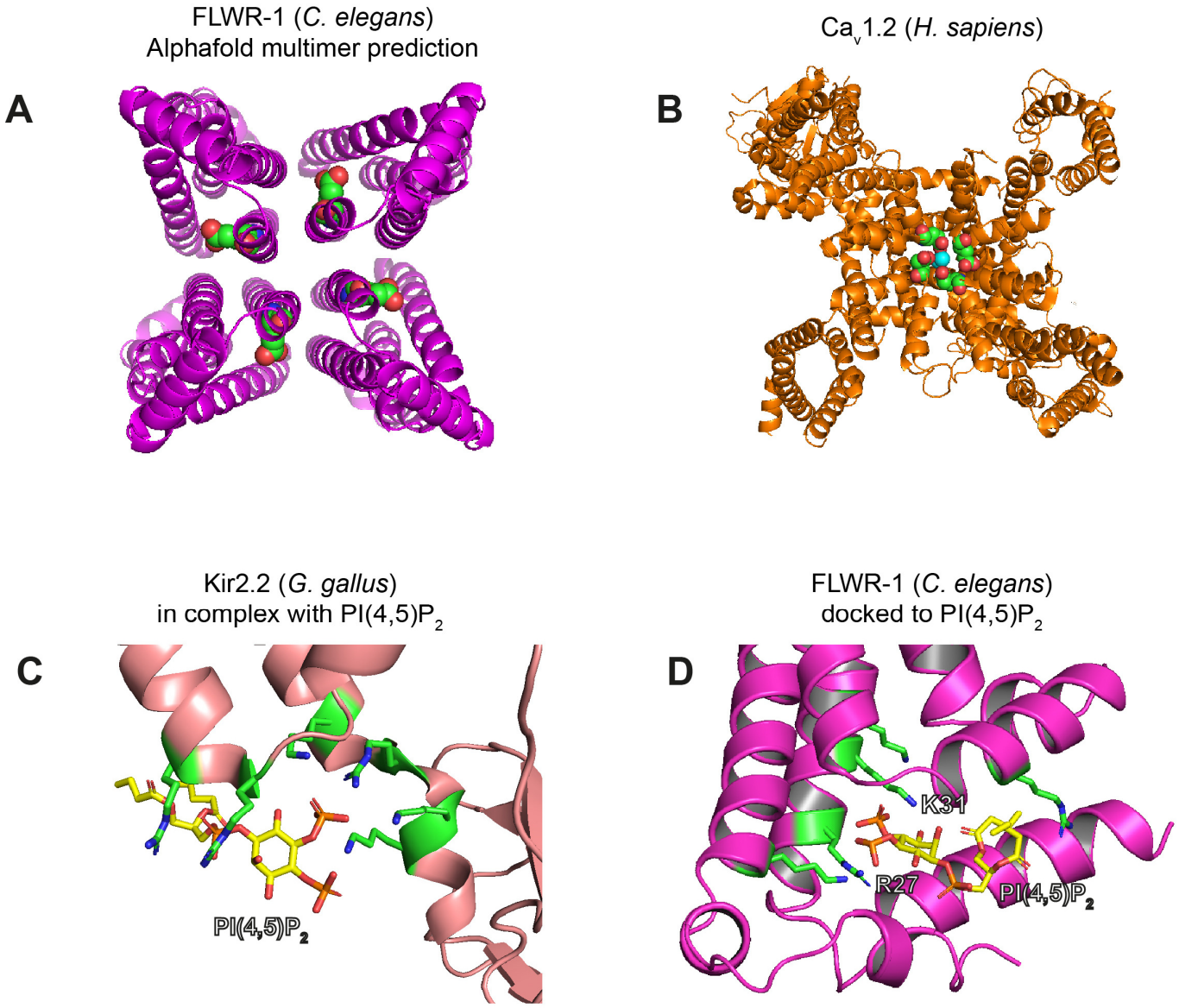

Fig. S7. Structural analysis of important amino acid residues in FLWR-1 and other proteins.

(A) Top view of an Alphafold3 prediction of a tetrameric FLWR-1 structure. Glutamate 74 is indicated as colored spheres in each monomer. **(B)** Cryo-EM structure of the human L-type voltage-gated calcium channel $Ca_v1.2$ (PDB: 8EOG) (Chen et al., 2023). Glutamate residues in the central pore are indicated as spheres. Ca^{2+} ions within the pore are depicted as turquoise spheres. **(C)** X-Ray structure of the Kir2.2 potassium channel in a complex with $PI(4,5)P_2$ (PDB: 3SPI) (Hansen et al., 2011). Basic amino acid residues in the proximity of $PI(4,5)P_2$ are depicted as sticks. **(D)** $PI(4,5)P_2$ was docked to the Alphafold3 structure of FLWR-1 using AutoDock Vina (Eberhardt et al., 2021). Basic amino acid residues in the proximity of $PI(4,5)P_2$ are depicted as sticks. Arginine 27 and lysine 31 are indicated.